A structural and stratigraphic study in Liuyuan area, Southern Beishan orogenic collage, Northwest China

by

Jiangyu Li

A thesis

presented to the University of Waterloo

in fulfillment of the

thesis requirement for the degree of

Master of Science

in

Earth Science

Waterloo, Ontario, Canada, 2019

AUTHOR'S DECLARATION

I hereby declare that I am the sole author of this thesis. This is a true copy of the thesis, including any required final revisions, as accepted by my examiners.

I understand that my thesis may be made electronically available to the public.

Abstract

A stratigraphic and structural study of the Permian North Shuangbaotang Complex offers new evidence constraining the timing of the final closure of the Paleo-Asian Ocean to the late Permian. The fold and thrust belt of turbidite sequence in the North Shuangbaotang Complex is interpreted as a syn-tectonic sedimentary deposit in a retro-foreland basin on the upper plate recording the termination of the final stage of accretionary orogenesis in the Beishan orogenic collage.

A reconstruction of stratigraphy and structural analysis in this study identified that the North Shuangbaotang Complex is composed of two fault- bounded sedimentary packages and one cover package, which are subjected by two phases of deformations. Package 1 is considered as a part of an accretionary wedge derived from the Liuyuan Complex and package 2 is a part of a forearc basin derived from the Dundunshan terrane. The northward subduction of the oceanic crust and early collision between the Dundunshan terrane and the Dunhuang terrane led to D_1 deformation characterized by southwesterly thrusting. The continuous collision thickened the orogenic wedge and promoted the uplift-driven erosion of packages 1 and 2. Hence a syn-tectonic foreland basin formed and unconformably overlied imbricated packages 1 and 2. D_2 deformation is represented by the north-verging fold and thrust belt in the retro-foreland basin and constrains the final stage of shortening in the southern Beishan orogenic collage to late Permian.

Acknowledgements

I thank my parents and friends for supporting and encouraging my study over the years. I appreciate that Drs. Wenhua Ji and Kai Wang of the China Geological Survey (Xian center) provided me geological documents of the study area. I also thank my colleagues Qihang Wu, Meiling Wu, Tong Hong, Xiucai Li and Hengzhong Qiao for their helpful discussions. Tong Hong is further thanked for collecting the SHRIMP U-Pb data reported in this thesis. John Waldron and Jian Zhang are thanked for advising me to proceed with additional geological mapping. Thank you Changcheng Li for your GIS support. Many thanks to my committee members, Brain Kendall, Chris Yakymchuk, Cees van Staal and Shoufa Lin. Especially I thank my supervisors Shoufa Lin and Cees van Staal for their great help in my Master's study.

Table of Contents

List of Figures vii

List of Tables ix

Chapter 1. Introduction 1

1.1 Introduction to the study area 1

1.2 Geological setting 2

1.3 Tectonic setting of the study area 5

1.4 Purpose of study 6

1.5 The framework of the thesis 7

Chapter 2. Lithology and stratigraphy of the North Shuangbaotang Complex 11

2.1 Introduction 11

2.2 Nature of the boundaries of the North Shuangbaotang Complex 11

2.3 Lithologies of the North Shuangbaotang Complex 12

2.4 Significant unconformities in the stratigraphy 22

2.5 Summary of the stratigraphy 23

Chapter 3. Structural analysis 34

3.1 Structural boundaries 35

3.2 Structural domains 37

3.3 Road-cut cross-section 41

Chapter 4. Geochronological constraints 53

4.1 Introduction 53

4.2 Analytical technique 53

4.3 Results of selected samples 54

Chapter 5. Tectonic interpretations of the stratigraphy and structures 64

5.1 Introduction 64

5.2 Interpretation of stratigraphy 64

5.3 Interpretation of structures 68

5.4 Tectonic history of this study 72

Chapter 6. Conclusion and Tectonic Implication 77

Reference 79

List of Figures

Figure 1-1 A map showing the location and extent of the CAOB. 8

Figure 1-2 A tectonic map of the Beishan orogenic collage. 9

Figure 1-3 Simplified geological map 10

Figure 1-4 A cartoon showing the final stage of subduction-accretion in the Liuyuan Ocean. 10

Figure 2-1 Geology map of the Liuyuan area. 25

Figure 2-2 Simplified stratigraphic column of the study area. 26

Figure 2-4 Photograph of the chaotic sediment in package 1 27

Figure 2-4 Greywacke of package 1 28

Figure 2-5 Photos of sandstone interbedded with conglomerate and chaotic 2 unit in package 2 29

Figure 2-6 Photos of turbidite and conglomerate in the cover package..... 30

Figure 2-7 Photo of outcrop showing the angular unconformity between a Permian conglomerate and a Late Carboniferous to early Permian limestone. 31

Figure 2-8 Photo of outcrop showing the angular unconformity between the cover package and package 1..... 32

Figure 2-9 Photo of young indicators of in study area. 33

Figure 3-1 Structural map of the study area. 44

Figure 3-2 Photos of of the Northern fault boundary. 45

Figure 3-3 Photos and sketch of the Internal fault boundary. 46

Figure 3-4 Equal area steronets for three structural domains. 47

Figure 3-5 Photo of domain A in road-cut cross-section 48

Figure 3-6 Photo of a reverse fault in domain B. 49

Figure 3-7 Photo of domain B showing boudinage of sandstone layer. 50

Figure 3-8 Photo of domain C in cross section. 51

Figure 3-9 A 144 m long road-cut structural cross-section of turbidite in the cover package 52

Figure 4-1 Photos of outcrop and thin sections for selected geochronological samples. 57

Figure 4-2 CL images for geochronological samples in study area. 58

Figure 4-3 Concordia diagrams for analyzed geochronological samples. 59

Figure 5-1 Original D_1 structures by unfolding F_2. 75

Figure 5-2 Tectonic model proposed in this study. 76

List of Tables

Table 4-1 SHRIMP U-Pb analysis for the rhyolite porphyry (Sample 16-LYJ-119A).. 60

Table 4-2 SHRIMP U-Pb analysis for the ash beds (Sample 16-LYJ-182) 61

Table 4-3 SHRIMP U-Pb analysis for the rhyolite porphyry boulder in package 2 (Sample 17-LYJ-20191A).. 62

Table 4-4 SHRIMP U-Pb analysis for the trondhjemite (Sample 16-LYJ-60B).. 63

Chapter 1.Introduction

1.1 Introduction to the study area

The Central Asian Orogenic Belt (CAOB) is one of the largest accretionary orogenic belts in the world (Fig. 1-1), representing an area of important crustal growth. Following the introduction of the theory of plate tectonics in the 1960s, a systematic tectonostratigraphic analysis demonstrated that the CAOB extended to the East European Craton in the west, Siberia Craton in the North, North China Craton and Tarim Craton in the south (Fig. 1-1). Decades of study showed that the CAOB was formed by multiple stages of northward accretionary tectonic events (Coleman, 1989; Sengör, Natal'in & Burtman, 1993; Dobretsov, Berzin & Buslov, 1995; Sengör & Natal'in, 1996; Gao et al. 1998; Buchan et al. 2002; Bazhenov et al. 2003; Xiao et al. 2003, 2004a, b, 2008; Windley et al. 2007). The termination of accretionary orogenesis in the CAOB is represented by the final closure of the Paleo-Asian Ocean. However, the timing of the final closure of the Paleo-Asian Ocean is still contentious.

The Beishan orogenic collage (BOC), located in the southernmost part of the CAOB between the Southern Tianshan suture zone to the west and the Solonker suture zone to the east (Fig. 1-1), was proposed by some workers to record the final closure of the Paleo-Asian Ocean (Xiao et al., 2010a; Mao et al., 2012b).

This thesis is focused on the structure and stratigraphy of the Permian sedimentary rocks in the Liuyuan area, which is located in the southern part of the BOC (Fig. 1-2). 120 km to the north of the Dunhuang City, an ENE-WSW trending basaltic belt of mafic rocks and Permian

sedimentary sequences are well exposed with little vegetation cover. This basaltic belt, referred to as the Liuyuan Complex, is exposed in the middle of the Liuyuan area and is considered as a dismembered Permian ophiolite by several workers in this area (Xiao et al., 2010a; Mao et al., 2012b). The emplacement of the Liuyuan ophiolite was proposed to constrain the timing of the final closure of the Paleo-Asian Ocean (Mao et al., 2012b).

1.2 Geological setting

As a product of the subduction-accretion system, the structure and the tectonostratigraphy of the study area is complex, mainly due to the superposition of multiple stages of tectonic events related to subduction, accretion and collision. There are three lithological domains present in the study area, which are summarized below from previous studies (Fig. 1-3). They are: 1) Permian ophiolitic assemblage (*Domain 1*), 2) Carboniferous – Permian sedimentary sequences and Permian volcanic rocks (*Domain 2*) and 3) Ordovician – Silurian granitic plutons and quartz-rich schist (*Domain 3*).

1.2.1 Lithological domain 1: Permian ophiolitic assemblage (Liuyuan Complex)

The ENE-WSW-trending Liuyuan Complex contains a typical ophiolitic assemblage comprising minor ultramafic rocks, pillow and massive basalts, gabbro, trondhjemite, tuffaceous sediments and marine chert (Mao et al., 2012b). Imbricated thrust sheets are well

developed within the extensive Liuyuan Complex (Mao et al., 2012b). The gabbro and basalt of the Liuyuan Complex display a supra-subduction zone (SSZ) geochemical signature (Mao et al., 2012b). Basalt within the Liuyuan Complex is generally metamorphosed to greenschist-faces conditions. Serpentine and epidote veins are common in the Liuyuan Complex.

1.2.2 Lithological domain 2: Carboniferous-Permian sedimentary units and Permian rhyolite

The Permian sedimentary lithologies on both southern and northern sides of the Liuyuan Complex display a similar detrital zircon age pattern (Cleven et al., 2017) and some similarities in sedimentary structures, but are different compositionally. To the north of the Liuyuan Complex, part of the turbidite sequence appears to represent a cover package to basalt, hence presumably form part of the Liuyuan Complex (Fig. 1-3). The Permian sedimentary rocks in the study area were previously grouped into the North Shuangbaotang Formation, which contains greywacke, siltstone, pebbly sandstone and some conglomerate (Guo et al., 2012). Sedimentary structures of turbidite deposits in the North Shuangbaotang Formation such as graded bedding, erosional base, parallel/cross-lamination, and scours are common, which represent elements of a classic Bouma sequence and characteristic of turbidite deposits. According to a published geological map, the Permian sedimentary sequences unconformably overlie Carboniferous limestones but are situated structurally underneath the Liuyuan Complex

(Gansu BGMR, 1966). Wang et al. (2017) considered the Permian sediments occurring in the North Shuangbaotang Formation to have formed in a rift basin, with comparable sedimentary lithologies on both sides of the Liuyuan Complex. However, the Permian turbidite deposits more likely formed in a convergent setting because the age of sediments overlaps the age of the folding and thrusting deformation (Cleven et al., 2017). The deformational structures encountered in the research area are characterized by fold and thrust belt. The overturning of bedding and cut-off structures created by thrusting are locally well preserved and described in more detail below (Chapter 4). The composition of the turbidite sequence comprises a significant volume of felsic volcanic clasts, inferred to have been derived from a nearby island arc. The detailed geochemical analysis from Guo et al. (2012) suggests that the provenance of the sediments in the North Shuangbaotang Formations includes an important component of continental / island arc rocks. A large body of rhyolite porphyry in the study area was previously interpreted as part of a Devonian volcanic arc, but SHRIMP dating of a rhyolite yielded a Permian age (See Chapter 4), hence it is a potential source for the volcanic-derived sediments.

1.2.3 **Lithological domain 3: Ordovician-Silurian granitic plutons and quartz-rich schist**

Further to the north, the North Shuangbaotang Formation (lithological domain 2) is juxtaposed with Ordovician - Silurian schist and a felsic to intermediate pluton (Fig. 1-3). The

pluton within the study area was recently dated at 424 ± 3 Ma by (Mao et al., 2012a). The pluton contains granodiorite, diorite, and granite. The quartz-rich schist in the study area is considered to form part of the southern margin of the Dundunshan terrane and is known as the Huaniushan Group (Xiao et al., 2010a). The Huaniushan Group records a complex pre-Permian tectonic evolution, including an association with 467 Ma eclogite in mafic rocks tectonically to the west of the Huaniushan Group (Qu et al., 2011). Liu et al. (2010) dated the relict zircon cores and constrained the age of protolith as ca. 1013 Ma to ca. 1002 Ma. The mafic protolith of the eclogite is thought to represent a subducted slice of MORB that returned to the surface prior to the Permian in a previous study (Xiao et al., 2010a).

1.3 Tectonic setting of the study area

The mapping area is tectonically situated between the Huaniushan group of the Dundunshan terrane to the north and the Shibanshan arc of the Dunhuang terrane to the south, documenting critical evidence of the closure of Paleo-Asian Ocean (Fig. 1-4).

The southern margin of the Dundunshan terrane contains ophiolitic mélange including gneiss, schist, mylonite, ultramafic rocks and turbidites (Zuo et al., 1990, 1991). Eclogites were identified within a belt of augen orthogneisses to the further west. Qu et al. (2011) dated the metamorphic age of eclogites as 465±10 Ma and considered the mafic protolith of the eclogite to represent a sliver of subducted oceanic crust (Xiao et al., 2010a). Calc-alkaline granitic

plutons were identified within the Huaniushan arc, which yielded a 380 ± 12 Ma U-Pb zircon age resulting from a Devonian intrusive event.

The Shibanshan arc on the Dunhuang terrane is interpreted as a continental arc by Mao et al. (2010a) and forms the southern margin of the BOC and immediately occurs to the north of Dunhuang block. Main rock units in the Shibanshan arc include granitic gneiss, schists, and migmatites. The ages of main rock units range from Devonian to Permian (Zuo et al., 1990; Zhao et al., 2006), but a significant volume is late Permian to Triassic in age. The granitic intrusion with late Permian to Triassic age is commonly observed in the Shibanshan arc.

1.4 Purpose of study

The timing of the terminal subduction-accretion events in the BOC are highly contentious. There are two main views regarding the termination of the successive subduction-accretion processes. The first view considers that the accretionary history of the BOC was finished before 300 Ma as a result of the collision of the Tarim and Kazakhstan plates (Han et al., 1998). Continental rifting occurred subsequently in the Permian. The second view considers the Permian tectonic setting to have involved subduction-accretion processes during the closure of the last vestige of the Paleo-Asian Ocean, principally based on the ophiolite interpretation of the Liuyuan Complex (Mao et al., 2012b). Moreover, there is no coarse grain rift basin sediments found within the Permian Liuyuan Complex (Mao et al., 2012b).

The two contrasting views discussed above are largely based on interpreting the tectonic setting of the igneous rocks. The structural and stratigraphic setting of the sedimentary rocks such as the turbidite sequences in our mapping area were, however, rarely taken into account. Therefore, this study focused on the structure and tectonostratigraphy of the Permian sediments, which was mapped in detail at a scale of 1:20,000 during this study.

1.5 The framework of the thesis

This thesis contains six main chapters. The first chapter is an introduction, which briefly introduces the regional geological background and summarizes the previous studies. The second chapter describes the different sedimentary units identified from the field investigations in a tectonic and/or stratigraphic order. Analysis of the structural history of the rocks and their relationships with adjacent rock units comprises the main content of the third chapter. Equal-area stereonet plots are used to identify and examine the structural histories and patterns of the various structural domains recognized. The fourth chapter describes the results of all geochronologically analyzed samples in this study. The fifth chapter discusses, interprets and combines all data into a tectonic model. The sixth chapter summarizes the conclusions of this study.

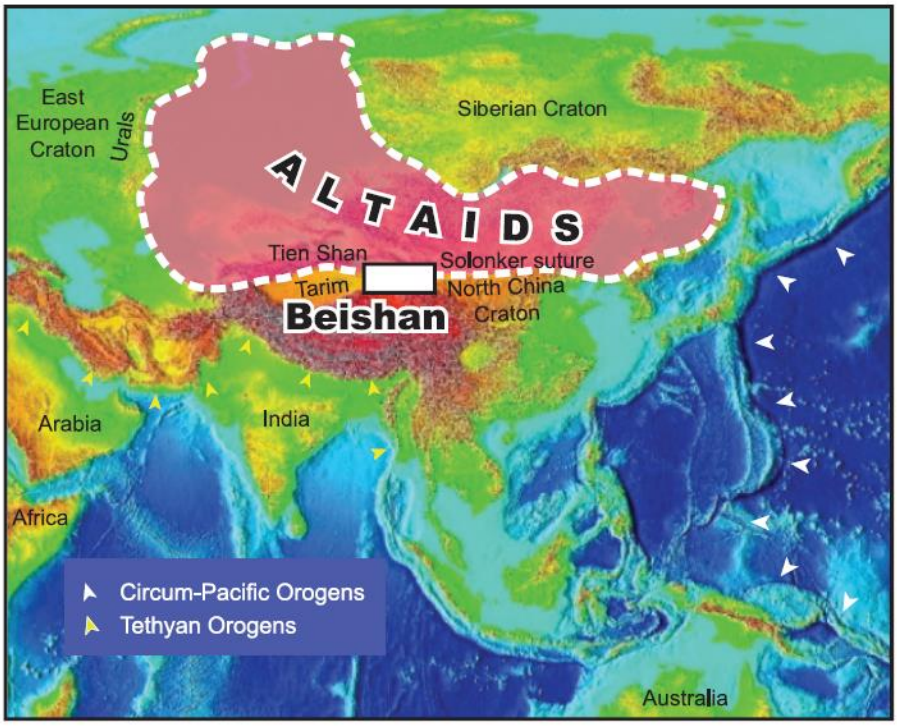

Figure 1-1 A map showing the location and extent of the Altaids, also known as Central Asian Orogenic Belt (CAOB). The Beishan orogenic collage (BOC) is located at the southernmost margin of the CAOB, indicated by the white box (From Xiao et al., 2011).

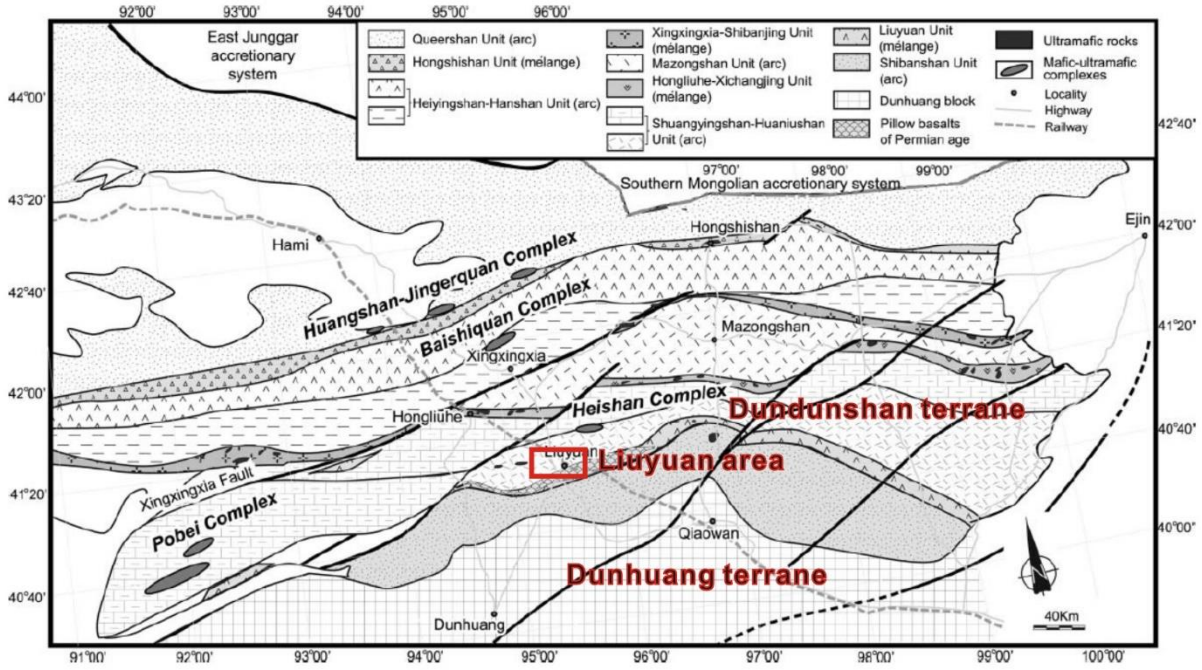

Figure 1-2 A tectonic map of the Beishan orogenic collage showing tectonic terranes and ophiolite slices. My study area is the Liuyuan area located in the southernmost of the BOC (From Xiao et al., 2010a).

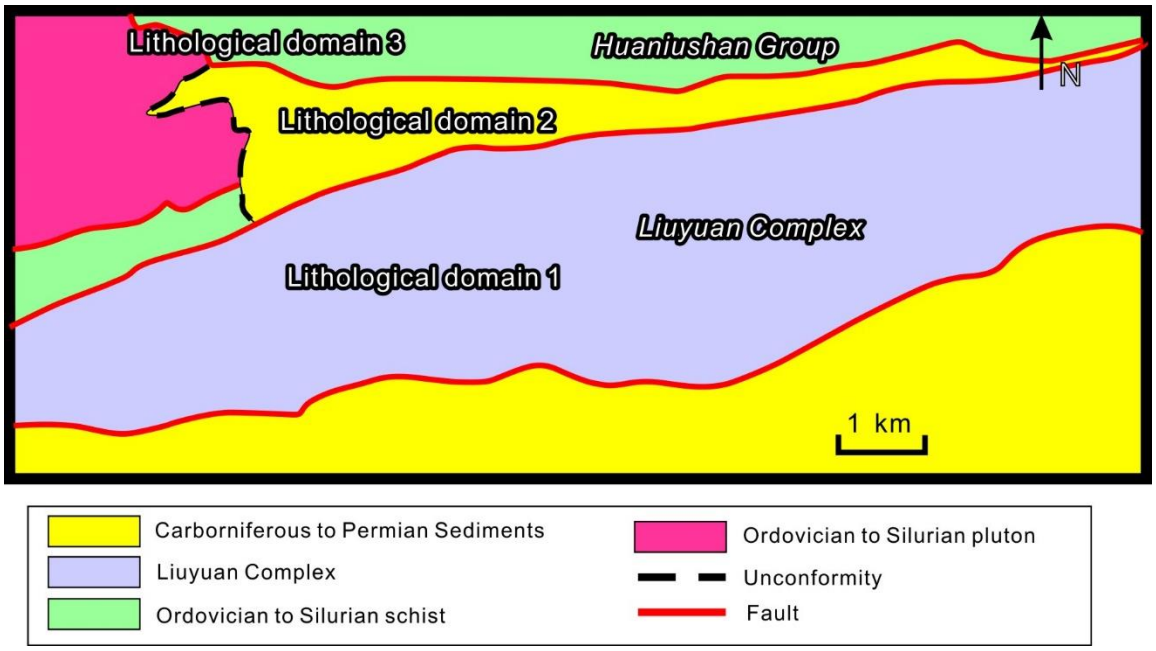

Figure 1-3 Simplified geological map showing the geological units in the mapping area. Modified from Gansu BGMR (1966).

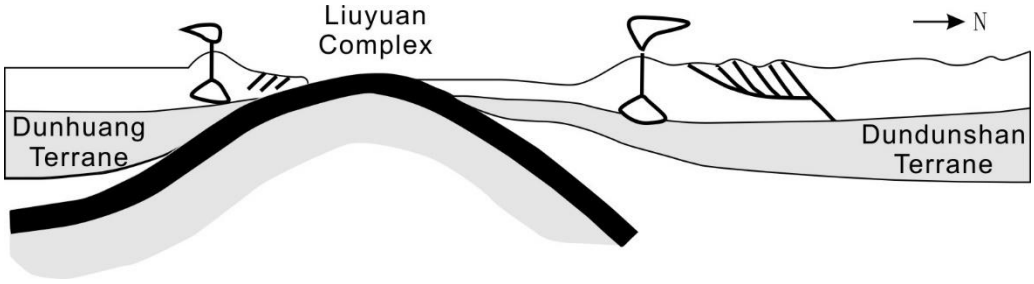

Figure 1-4 A cartoon showing the final stage of subduction-accretion in the Liuyuan Ocean. The Liuyuan Ocean is closed by the collision between the Dunhuang terrane and Southern margin of the Dundunshan terrane. Modified from Xiao et al. (2010a).

Chapter 2. Lithology and stratigraphy of the North Shuangbaotang Complex

2.1 Introduction

The sedimentary rocks in the study area were previously included in the North Shuangbaotang Formation. The latter formation is renamed into a complex in this study because its various sedimentary constituents do not form a coherent stratigraphic unit. The 1:20,000 scale geological mapping conducted in this study covered an area of 200 km^2 and has led to a better understanding of the tectono-stratigraphic make-up of the North Shuangbaotang Complex. The new geological map produced in this study divided the study area into two sedimentary packages bounded by faults and, at least in part, unconformably overlain by a package of turbidite and conglomerate (Fig. 2-1 and Fig. 2-2).

2.2 Nature of the boundaries of the North Shuangbaotang Complex

The North Shuangbaotang Complex is bounded between two major fault contacts along its northern and southern boundaries, with the Ordovician quartz-rich schist of the Huaniushan Group and the Permian Liuyuan complex, respectively (Fig. 2-1).

The northern boundary of the Permian North Shuangbaotang Complex is here named the Northern Fault. It steeply dips to the north, with the Ordovician schist and mylonite in the hanging wall, thus placing old over young (Fig. 2-1) (See Chapter 3).

The southern boundary of the North Shuangbaotang Complex is named the Southern Fault. It also steeply dips to the north. The fault emplaced the Permian North Shuangbaotang Complex and the Ordovician quartz-rich schist above the Liuyuan Complex (Fig. 2-1). The Southern Fault was not well understood in previous studies and will be described and discussed in more detail in Chapter 3.

2.3 Lithologies of the North Shuangbaotang Complex

The study area is underlain by two diverse rock packages that are in fault contact. Each package comprises several different lithological units. The two packages are covered by a sedimentary package containing turbidite and conglomerate (Fig. 2-1). The two lower packages are 1) The Permian Liuyuan Complex and covering sedimentary rocks and 2) Ordovician to Silurian quartzitic rocks of Huaniushan Group (BGMR,1966), Ordovician to Silurian granite to intermediate plutonic rocks, Carboniferous to Permian limestone, Permian sandstone and conglomerate and chaotic sediments containing rhyolite boulders. The volcanic rocks in the northern part of the study area comprises porphyritic rhyolite. The relationships between the rhyolite with each package is complex due to the structural overprint.

2.3.1 **Package 1**

Package l in the study area contains pillow basalt, chaotic sediments, and sandstone (Fig. 2-1 and Fig. 2-2). The pillow basalt is the basement to package 1 and inferred to be part of the nearby Liuyuan Complex. The chaotic sediments in package 1 mainly comprise basaltic boulders in a dark mudstone matrix (Fig. 2-3) without coherent bedding. A unit of greywacke conformably overlies the chaotic sediments and displays coherent sedimentary bedding.

Basaltic basement

An isolated slice of the pillow basalt in the southern part of the mapping area is considered the basement to the package 1. Pillows, where well preserved, show northward younging directions, suggesting the basalt slice has a northernly dip. Basalts are metamorphosed to green schist facies conditions, because the primary igneous minerals including plagioclase and pyroxene, were altered to epidote, chlorite, sericite and albite. This basaltic basement maybe part of the nearby Liuyuan Complex but further study is needed to confirm this. The age of the Liuyuan Complex is constrained by a ca. 285 Ma trondhjemite intrusion (See Chapter 4), but the basalt of package 1 may be older if it comprises a piece of crust of the oceanic basin in which the suprasubduction zone Liuyuan Complex formed.

Chaotic sediments

Chaotic sediments in package 1 are mainly composed of fragments of pillow basalt and sandstone and mudstone matrix. The pillow basalt is sheared and wrapped around by the foliated mudstone due to competency contrast (Figs. 2-3a and 3b). The prefer orientation of the pillow basalt is parallel with the foliation of the mudstone in the matrix. The pillow basalt is amygdular with the vesicles filled by calcite (Fig. 2-3c). There is no coherent bedding in the mudstone matrix. The contact relationship between the chaotic sediments and underlying basalt is tectonic contact because basaltic fragments of chaotic sediments were derived from underlying basement. The chaotic sediments are interpreted as tectonosome based on two important features: 1) block in matrix pattern 2) strong ordered feature (See Chapter 5) (Pini, 1999).

Greywacke

The main component of the sandstone unit is a greywacke with minor mudstone component. Greywacke is composed of quartz (45%), feldspar (25%), lithics (15%) and sericite (15%). Since the sericite is mainly produced by the sericitization of the feldspar, the original content of feldspar in the sandstone may have been up to 40%. Clasts of olivine, pyroxene, chert and minor volcanic lithics were observed under microscope (Figs. 2-4b, 2-4c and 2-4d) suggesting a mafic provenance. Basalt clasts also occur within the sandstone in

outcrop, which further confirms that the basalt and associated mafic rocks of the Liuyuan Complex are likely provenance of the greywacke (Fig. 2-4a).

The contact relationship between the greywacke and chaotic sediments is conformable. Bedding gradually becomes more coherent upwards from the chaotic sediments to the overlying greywacke rather than with a sharp boundary. Bedding of the sandstone near the boundary is dipping and young towards the north based on erosional base (Figs. 2-9a and 2-9b). On the west side of package 1, the sandstone unit unconformably overlies the basalt. The abundance of basalt clasts in the sandstone indicates that erosion of basalt preceded the deposition of the greywacke.

The angular grain shape and the high abundance of feldspar indicate the greywacke has a low maturity close to source area.

2.3.2 **Package 2**

Package 2 comprises Ordovician to Silurian quartz-rich schist of the Huaniushan Group, granite to intermediate pluton, limestone, sandstone interbedded with conglomerate and chaotic sediments containing various types of boulders including porphyritic rhyolite (Fig. 2-1 and Fig. 2-2). The Ordovician to Silurian metamorphic rocks represent the basement to the unconformably overlying sedimentary rocks. Carboniferous to Permian limestone unconformably overlies the Ordovician to Silurian metamorphic basement and the associated

felsic to intermediate pluton. The unit of sandstone interbedded with conglomerate unconformably overlies the Carboniferous to Permian limestone. This unconformity is angular (Fig. 2-7). The youngest unit of package 2 comprises chaotic sediments, which contains rhyolite boulders and sandstone blocks. These rhyolite boulders are coeval with a rhyolite unit in the northern part of the mapping area (see Chapter 4), which I interpret, together with spatially associated ash beds, to sit in the same stratigraphic horizon as the package 2 sediments (Fig. 2-2).

Ordovician to Silurian quartz-rich schist

The Ordovician to Silurian quartz-rich schist of the Huaniushan Group forms the basement to the sedimentary rocks of package 2, which is juxtaposed with the turbidite of the cover package to the north and Liuyuan Complex to the south. Along the northern boundary of the North Shuangbaotang Complex, quart-rich schist is steeply dipping toward the north. Along the northern boundary of the Liuyuan complex, the northward dipping quartz-rich schist structurally overlies the Liuyuan Complex.

Ordovician to Silurian pluton

The Ordovician to Silurian gneissic granite intruded into the quartz-rich schist in the study area, which is mainly composed of plagioclase, quartz, biotite and hornblende (Mao et al., 2012a). The contact relationship between Ordovician to Silurian pluton and overlying Carboniferous to Permian limestone is an unconformity.

Carboniferous to Permian limestone

The Carboniferous to Permian limestone unit has a dark grey color and comprises a thin layer overlying both the Ordovician to Silurian quartz schist and pluton. The age of limestone is constrained by fossils, such as *Marginifera* sp., *Cleiothyridina* sp., and *Rhynchonellids* (Gansu BGMR, 1966; Guo et al., 2012).

Sandstone interbedded with conglomerate

The sandstones of package 2 are dominated by arkosic sandstone and locally interbedded with conglomerate (Fig. 2-5a). The bedding of sandstone is generally dipping towards the east and young eastward, as evidenced by graded bedding (Fig. 2-5e). Arkosic sandstone is green at the bottom of the unit and gradually changes to red near the top. The change in color may reflect a shallowing of the water depth of deposition. The sandstone is dominated by quartz and feldspar (Fig. 2-5f). The high abundance of quartz indicates relatively high compositional maturity. However, the poor sorting and angular shape of the quartz clasts indicates a short distance of transportation. Both sandstone and conglomerate are well stratified with beds having thickness of up to tens of centimeters. The clasts within the conglomerate display slight alignment, which is inferred to indicate the paleo-current flow direction (Fig. 2-5c). The rhythmic repetition of sandstone and conglomerate suggests deposition in an alluvial fan setting.

Petrographic analysis revealed that the conglomerate of package 2 contains ca. 40% quartz and more than 50% of rock fragments. The sandstone is mainly composed of quartz (40%) and feldspar (>30%). Clasts in the conglomerate include quartz-rich schist, rhyolite and sandstone. The rhyolite clasts are characterized by a high amount of quartz and feldspar (Fig. 2-5e). The sandstone and conglomerate in package 2 are more felsic than the sandstone in package 1. In addition, there are no basaltic clasts found within package 2.

Chaotic sediments in package 2

The chaotic sediments in package 2 are typical of olistostrome deposits, which are characterized by a great internal heterogeneity and discontinuous bedding (A. Festa et al., 2016). The chaotic sediments of package 2 were mainly derived from the underlying unit of sandstone interbedded with conglomerate, because fragments of interbedded sandstone and conglomerate were identified in the chaotic sediments.

There are at least 3 types of boulders identified within the chaotic sediments of package 2. Type 1 boulder is conglomerate derived from the underlying rocks, which is well stratified and contains alignment of clasts (Fig. 2-5c). Petrographic examination reveals that type 1 boulders consist of around 50% quartz, 30% lithic and 20% feldspar. Type 2 boulder is arkosic sandstone (Fig. 2-5f). Type 3 boulder is porphyritic rhyolite, which shares the same age with the rhyolite unit in the north part of the study area (Fig. 2-5b and 2-5d). Recent SHRIMP U-Pb zircon dating determined the age of the rhyolite boulder as ca. 279 Ma, which constrains

the formation age of the chaotic sediments to 279 Ma or younger, but before the deposition of the cover package (See Chapter 4).

2.3.3 **Volcanic rocks**

A volcanic unit of rhyolite porphyry and spatially associated ash beds is located in the northern part of the study area. The contact relationship between the volcanic unit and packages 1 and 2 is not observed in the field. The only linkage between the volcanic unit and package 2 is that rhyolite unit shares the same age with the rhyolite boulders in the chaotic sediments of package 2. Structure suggests the rhyolite porphyry together with the ash beds occupies the northern limb of a shallowly east plunging synform (Fig. 2-1) and connects to package 2 at depth beneath unconformable cover package.

Rhyolite porphyry

The rhyolite prophyry is characterized by a porphyritic texture (Fig. 2-5d) and pervasive flow banding. The SHRIMP U-Pb dating yields an age of 282.2 $\pm$ 2.1 Ma (See Chapter 4).

Ash beds

A unit of ash beds is interbedded with siltstone in the northwestern part of the study area. The ash beds are deformed into a tight upright synform, immediately south of the rhyolite porphyry, which, together with the ash beds, are bounded to the north by the Northern fault, the trace of which is well displayed on the satellite image. U-Pb zircon dating of the ash beds

yielded an age of ca. 282 Ma (See Chapter 4), indicating a consanguineous relationship with the associated rhyolite magmatism, since the ages are coeval.

2.3.4 **Cover package**

Cover package comprises Permian turbidite and overlying polymictic conglomerate. The turbidite sequence mainly comprises arkosic sandstone.

Permian turbidite sequence

The turbidite sequence in the cover package comprises interbedded sandstone and siltstone characterized by abundant primary structures, such as graded bedding, parallel laminae, ripple laminae, and erosional base (Figs.2-6b, 2-6c and 2-9c). Those primary structures are typical features of turbidite deposits. This sedimentary sequence contains T_A, T_B and T_C components of the Bouma sequence. A few beds of turbidites are overturned (Figs. 2-13c and 2-13d). The SW dipping beds young towards the NE, evidenced by graded bedding in Fig. 2-9d. The best younging indicators of turbidite 2 are scour structures developed along the base of the sandy layers. Based on the scour structures in Fig. 2-9f, the NW-dipping turbidite is younging towards the northwest.

The turbidite is dominated by arkosic sandstone containing 60% feldspar, 30% quartz and 10% lithics. The quartz component is dominated by monocrystalline quartz. The components of the brownish-yellow arkosic sandstone are cemented together by quartz with an average

grain size of 0.3 mm. The feldspar-content comprises more plagioclase with albite twining than alkali feldspar (Fig. 2-6e). The rest of the lithics are mainly derived from nearby volcanic rocks, such as rhyolite (Fig. 2-6d). The relatively higher fraction of feldspar and its angular shape indicate lower compositional maturity and a short transportation distance from the source area to the site of deposition.

The western part of the turbidite is compositionally more calcareous. Calcareous sandstone in the field is characterized by a brownish-yellow weathering color and easy scratching. The carbonate cement is characterized by calcite and ankerite within thin sections. The formation of carbonate cementation depends on a constant supply of $CaCo_3^-$ which is pumped through the near-surface sediments by upward moving fluids (Boggs, 2009). Early Permian *Spiriferellasaranae* (Verneuil), *Kochiproductus porretus* (Kutorga), *Waagenoconcha* sp., *Neospirifer* sp., and *Athyris* sp. were identified within the calcareous sandstone by previous studies (Liao and Liu, 2003; Gansu BGMR, 1966). These early Permian fossils confirm a marine sedimentary environment.

This Permian turbidite sequence unconformably overlies package 1 by an angular unconformity described in more detail below in Section 2.4.

Conglomerate

The polymictic conglomerate in the cover package contains clasts of quartz, feldspar, sedimentary lithics, felsic and mafic volcanic lithics (Fig. 2-6f). The conglomerate is clast

supported with the grain size ranging from 0.3 cm-3 cm. The poor sorting of the conglomerate and its various composition indicate that the conglomerate is close to the source area.

2.4 Significant unconformities in the stratigraphy

Angular unconformity between the Carboniferous to Permian limestone and Permian sandstone interbedded with conglomerate of package 2

The sandstone in package 2 is overturned where it overlies the limestone in package 2. It dips towards the southeast and youngs northwestwards (Fig. 2-7). The bed of limestone is dipping to the southeast as well but with a shallower dip angle of ca. 45 degrees, which marks an angular unconformity. The angular unconformity was subsequently overturned due to later deformation.

Angular unconformity between the cover package turbidite and packages 1 and 2

This angular unconformity is demonstrated by turbidite of the cover package cutting the underlying, more steeply dipping sandstone of package 1 (Fig. 2-8). The basal conglomerate of the overlying turbidite near the contact has the same composition as the underlying sandstone of package 1, which indicates that the underlying sandstone was eroded before deposition of the overlying Permian turbidite of the cover package (Fig. 2-9). The map pattern

suggests a discordance between the F_2 folded ash beds and the overlying cover package turbidites along the northwestern limb of the F_2 synform recognized in the cover package (see Fig.3-1 in Chapter 3). Sandstone beds in package 2 dip steeply in the hinge area of the steeply east-plunging F_2 antiform, whereas the overlying turbidite beds of the cover package dip much more shallowly, also suggesting the presence of a pre-F_2 unconformity between package 2 and the cover package.

2.5 Summary of the stratigraphy

By combining the younging indicators and recent geochronological dating, a simplified geological column was built to indicate the relationship between two sedimentary packages and the overstepping sequences of turbidite and conglomerate (Fig. 2-2). Package 1 and its basaltic basement are in thrust fault contact with package 2 and both were subsequently unconformably overlain by the turbidite and conglomerate of the cover package. The thrust nature of the fault contact between packages 1 and 2 is based on two lines of evidence: 1) Basalt (>285 Ma) of package 1 structurally overlies younger chaotic sediments of package 2 (<279 Ma), and 2) shear sense indicators identified near shear zone indicate basalt of package 1 was thrust over chaotic sediments of package 2 (See Chapter 3). The depositional age of the turbidite of cover package is constrained by its youngest detrital zircon of ca. 277 Ma by

Cleven et al. (2017), and the 282-279 Ma age of the underlying rocks of package 2 and the associated volcanic rocks.

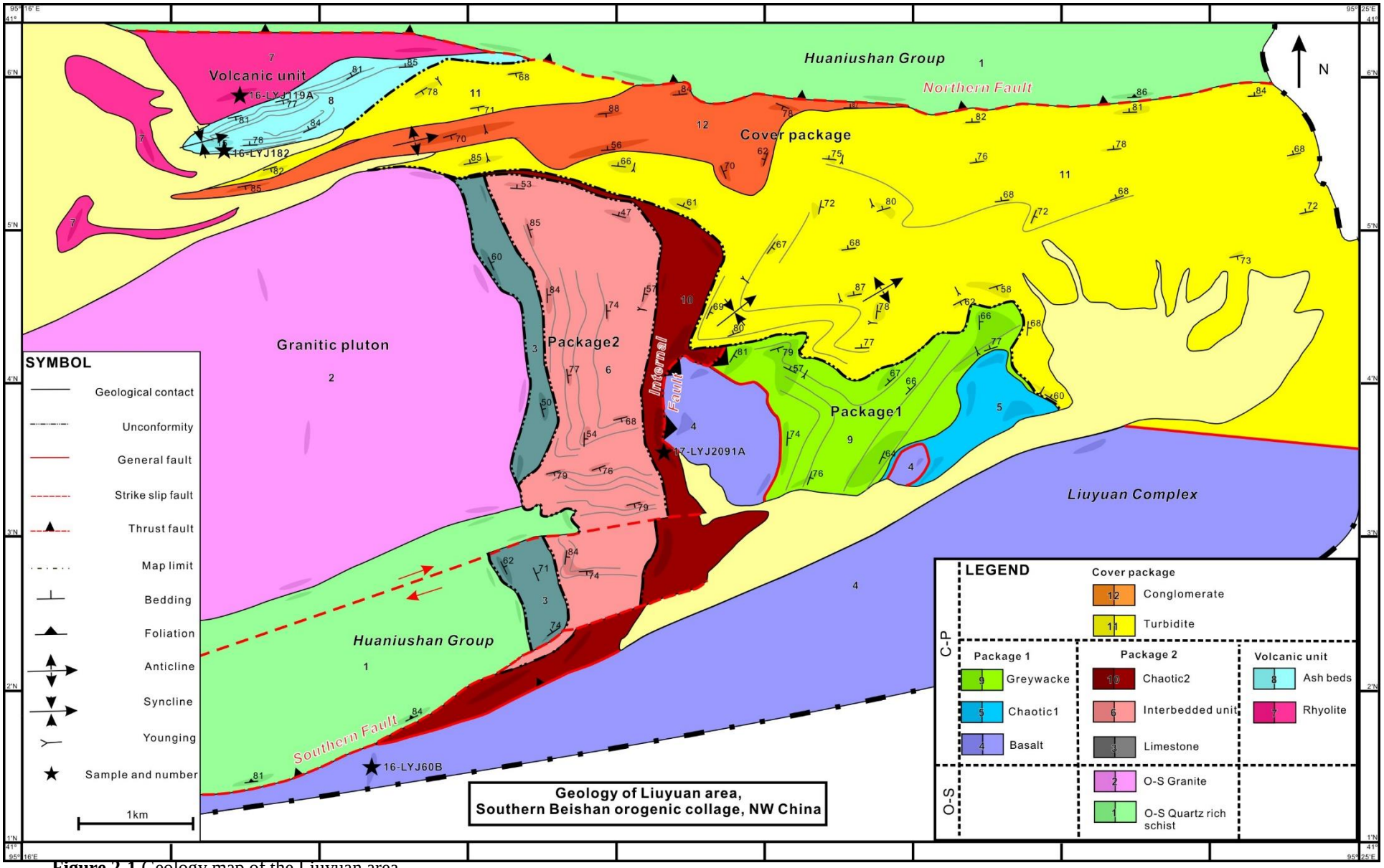

Figure 2-1 Geology map of the Liuyuan area.

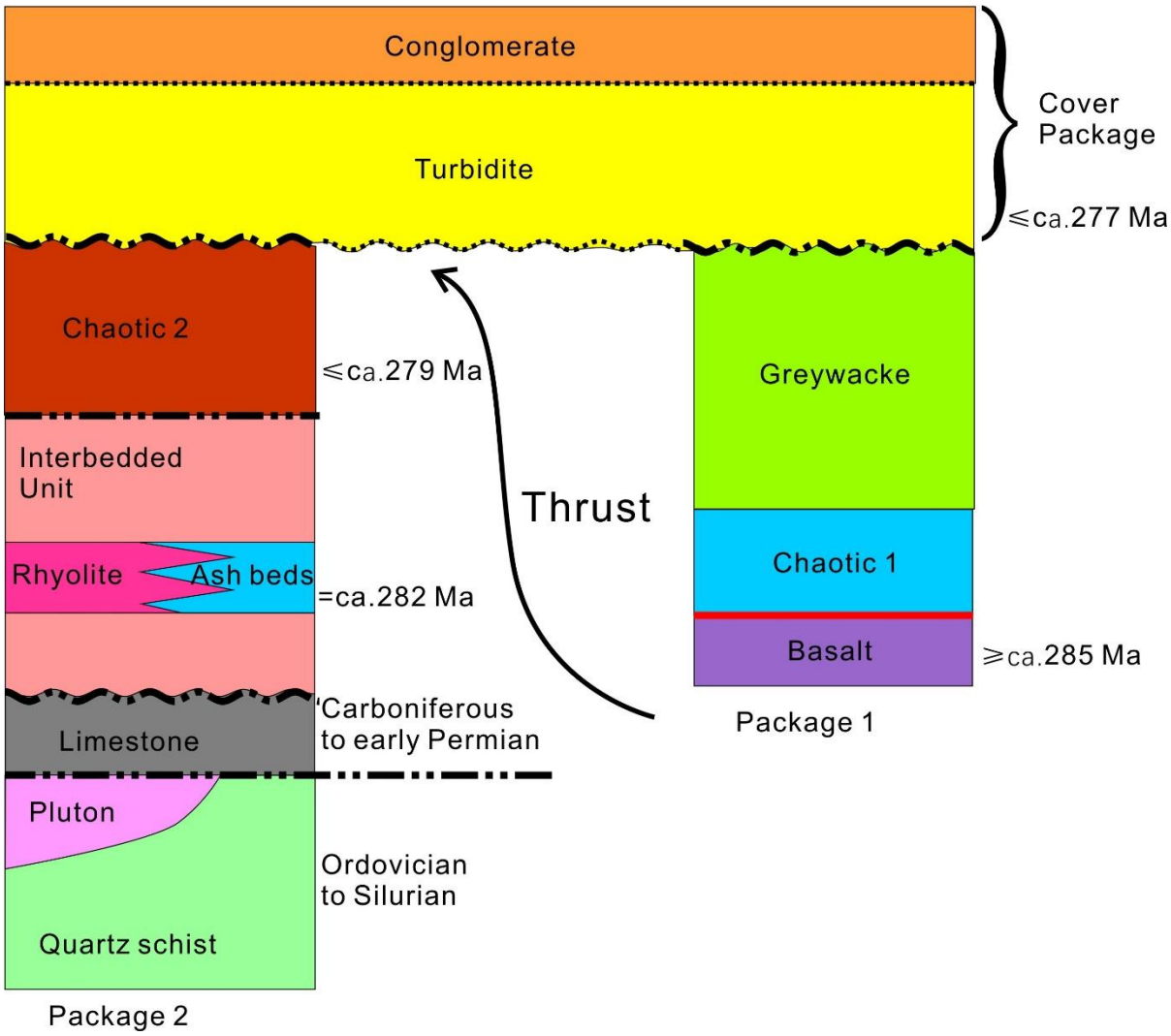

Figure 2-2 Simplified stratigraphic column of the study area. The packages 1 and 2 are in fault contact. The turbidite of the cover package unconformably overlies packages 1 and 2 and their fault contact. The Permian interbedded unit contains sandstone interbedded with conglomerate.

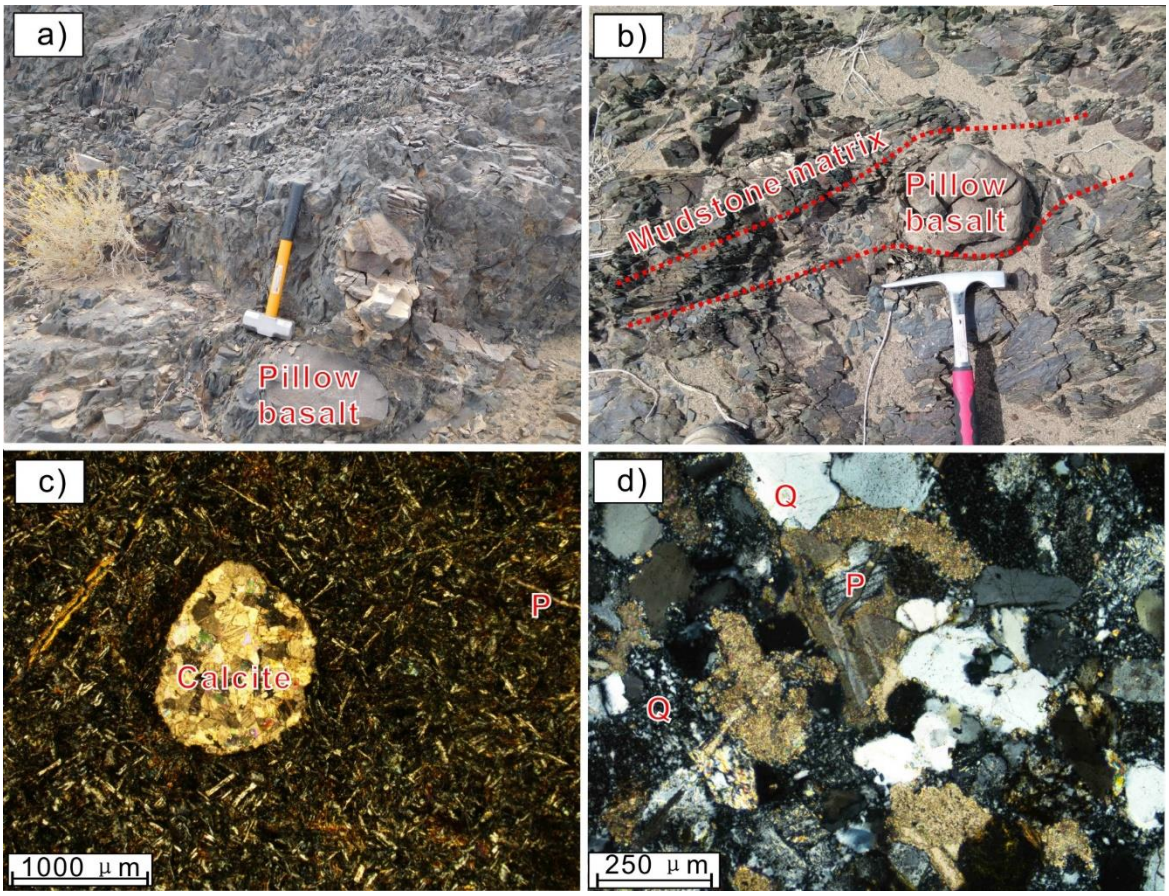

Figure 2-3 Photograph of the chaotic sediment in package 1. a) Block in matrix pattern. b) A pillow basalt is oriented and parallel with the foliation of mudstone matrix. c) Photomicrograph showing calcite amygdale within basalt. d) Photomicrograph of a fine grain sedimentary rock. Abbreviations: Q, Quartz; P, Plagioclase.

Figure 2-4 a) Greywacke of package 1 contains high volume of basaltic clasts. b) Photomicrograph showing an olivine and pyroxene clasts in greywacke of package 1. c) Photomicrograph showing angular felsic volcanic clasts in greywacke. d) Photomicrograph showing pyroxene clast within greywacke. The pyroxene clast develops a relic texture. Abbreviations: Q, Quartz; P, Plagioclase; Py, pyroxene; O, Olivine; Lv, volcanic lithic fragment.

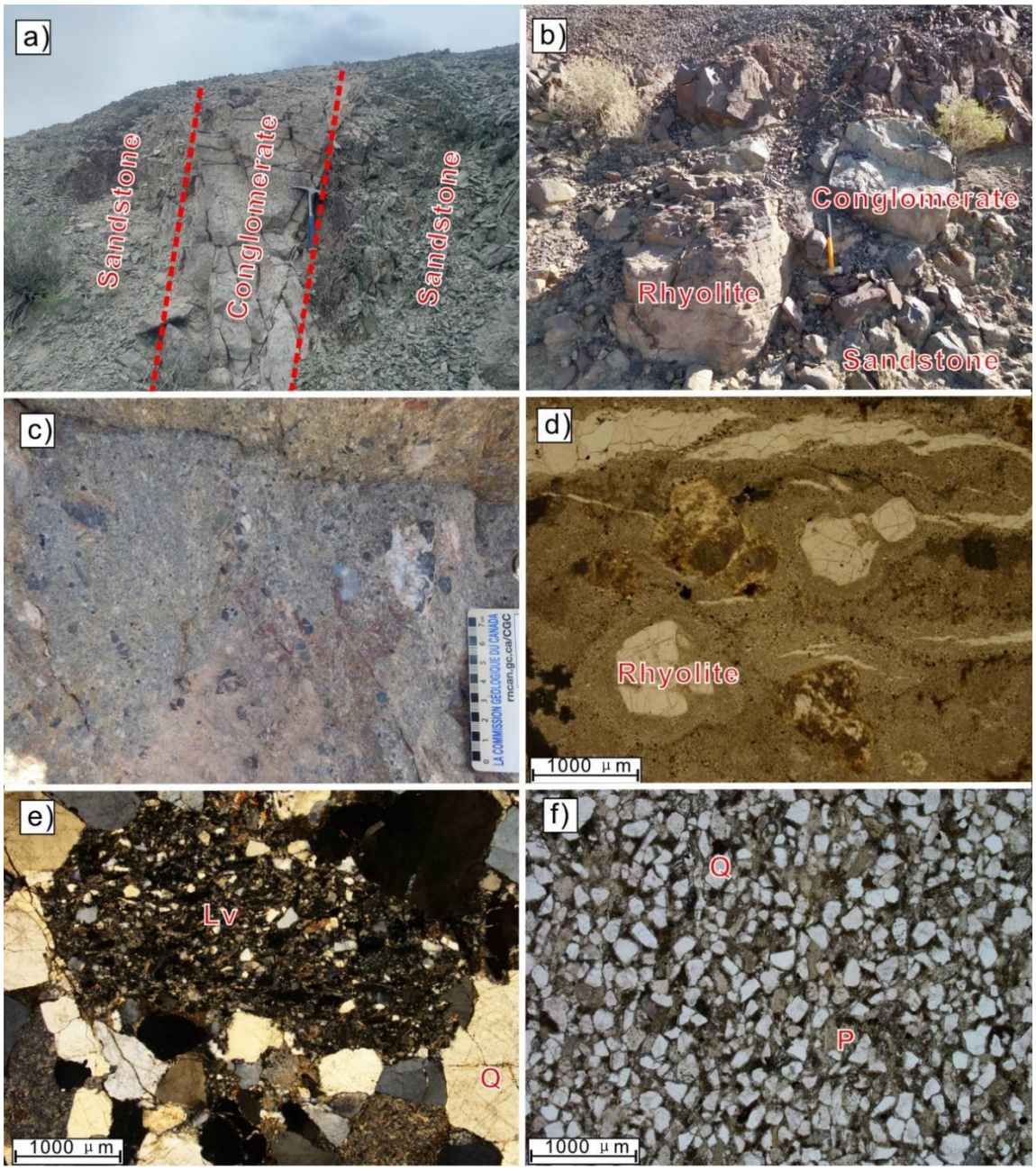

Figure 2-5 a) Photo showing sandstone interbedded with conglomerate. b) Photo showing the chaotic sediments of package 2 containing rhyolite, conglomerate and sandstone boulders. c) Close-up photo of the conglomerate boulder showing the alignment of clasts. d) Thinsection showing rhyolite porphyry in chaotic sediments of package 2. e) Photomicrograph showing a felsic volcanic lithic fragment from the sandstone. f) Photomicrograph showing the sandstone is dominated by quartz and feldspar grains. Same abbreviations.

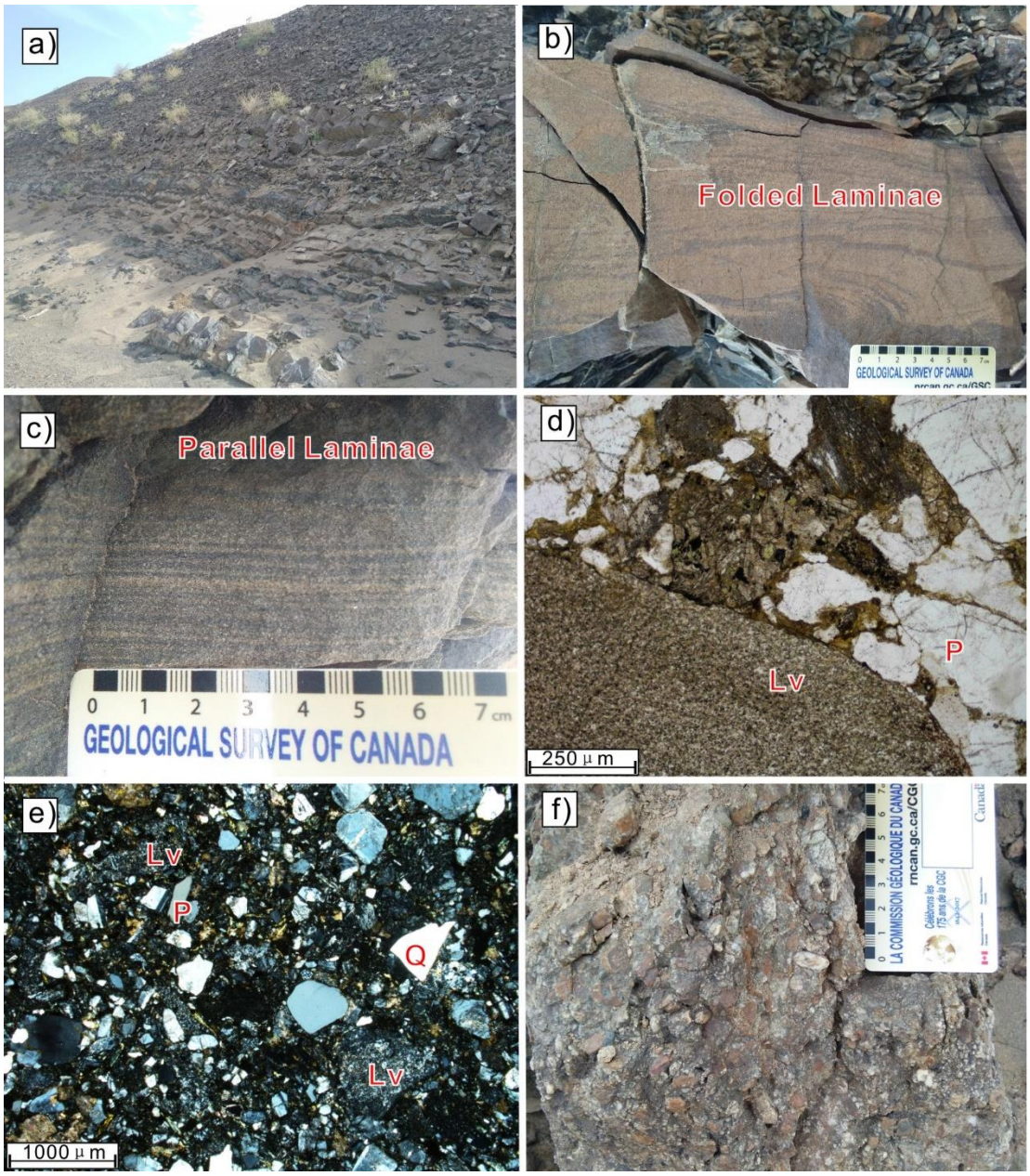

Figure 2-6 a) Photo of a turbidite in the cover package showing the interlayer of sandstone and siltstone. b) Photo of turbidite showing ripple lamination. c) Photo of turbidite showing parallel lamination. d) Photomicrograph showing felsic volcanic lithic fragments within turbidite. e) Photomicrograph showing plagioclase with albite twins within turbidite. f) Photo of outcrop showing conglomerate with abundant felsic volcanic clasts. Same abbreviations.

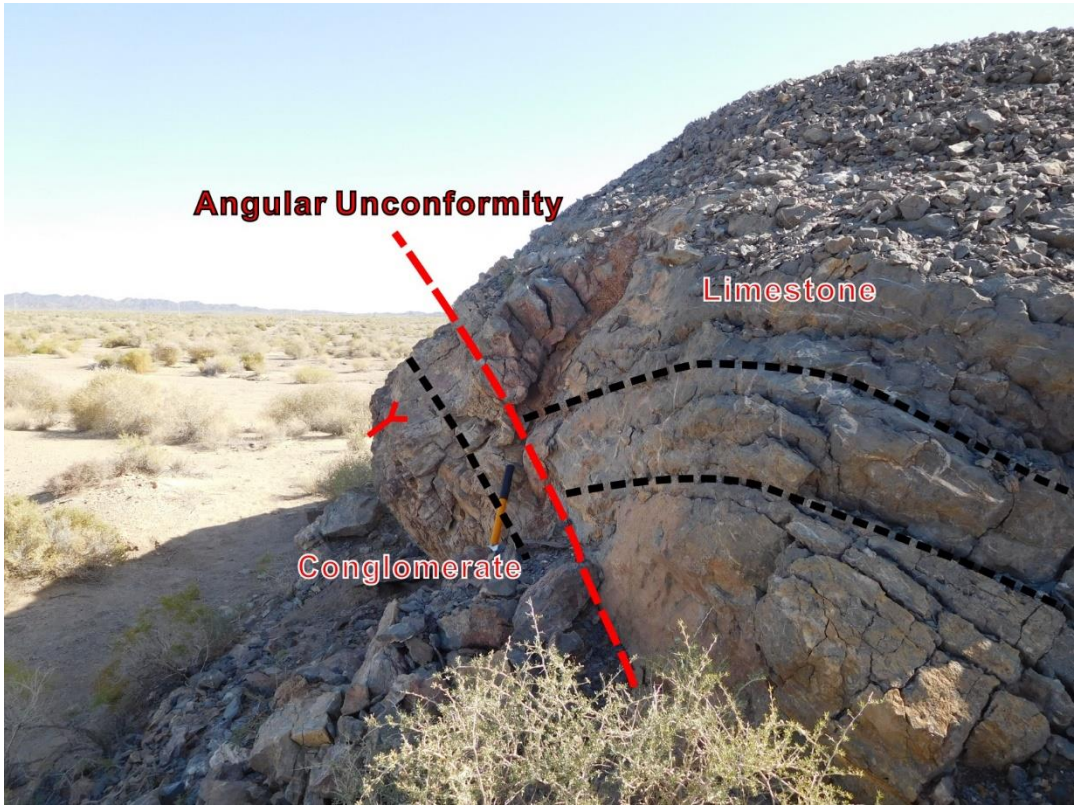

Figure 2-7 Photo of outcrop showing the angular unconformity between a Permian conglomerate and a Late Carboniferous to early Permian limestone. The limestone is overturned and structurally overlies the conglomerate.

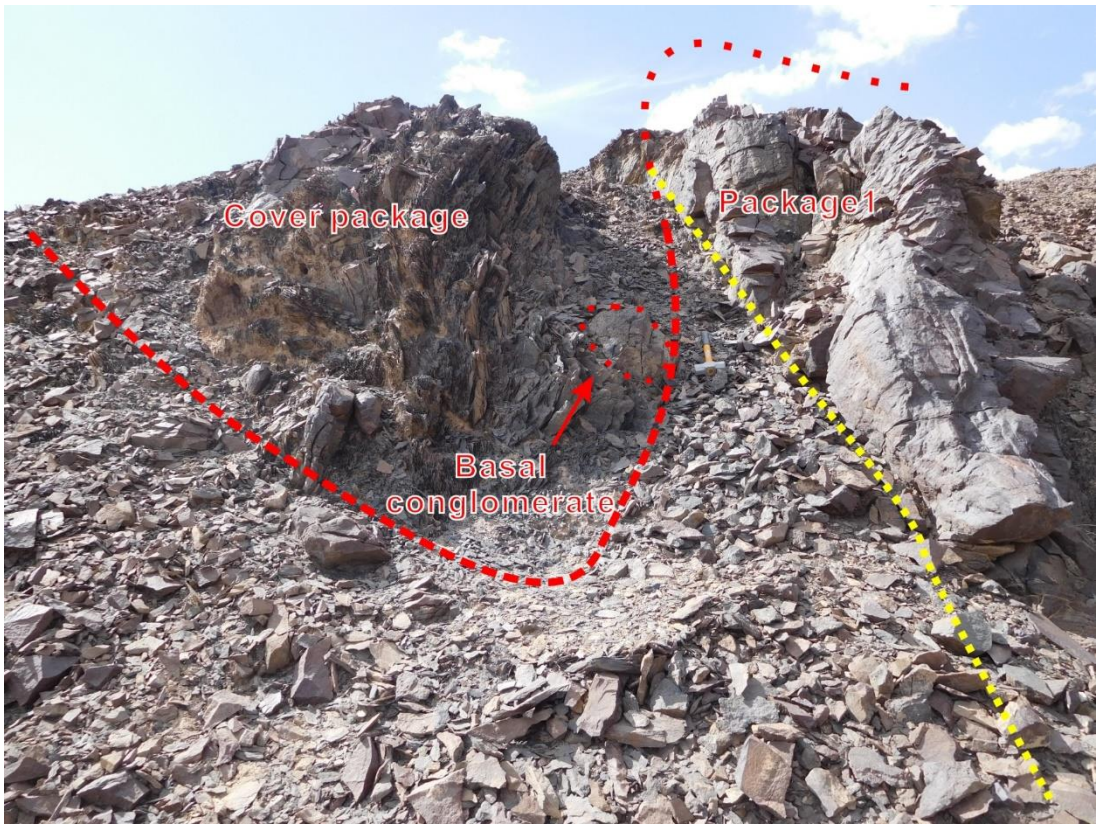

Figure 2-8 Photo of outcrop showing the angular unconformity between the cover package and package 1. Basal conglomerate boulders are found near the contact.

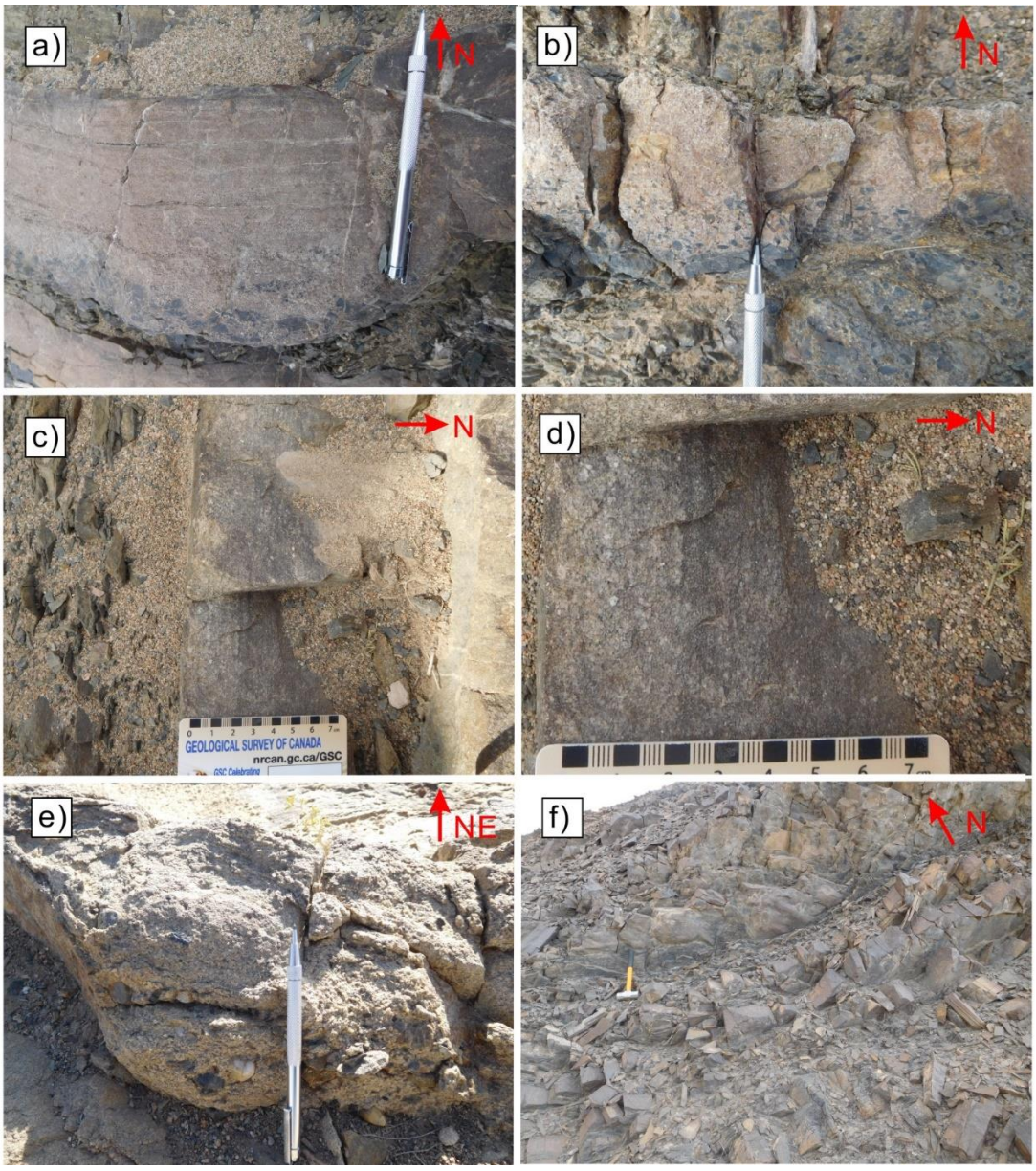

Figure 2-9 Photo of outcrops showing young indicators of sedimentary packages in study area. a) and b) are photos showing erosional base of turbidite in package 1. c) and d) are photos showing grade bedding of turbidite in cover package. E) Photo showing graded bedding of conglomerate in package 2. f) Photo of scour structures of turbidite in cover package.

Chapter 3. Structural analysis

Understanding the structural evolution and geometry of the deformed rocks is vital for understanding how, why and when the sedimentary rocks were deformed and translated into their present setting during orogenesis. The structure of the cover package in the investigated area is characterized by a large east-plunging D_2 anitform-synform pair. On a smaller scale the cover package rocks show a 'fold and thrust belt' style of deformation, evidenced by excellent exposures in a road-cut cross section (see Section 3.3) The outcrop scale north-verging fold structures and very low-grade metamorphism indicate that the cover package was likely subjected to thin-skinned deformation internally.

In the previous sections, packages 1 and 2 discussed herein were shown to be exotic to each other before their structural juxtaposition because they were derived from different sources and are in fault contact. Here, the structural analysis combined with the stratigraphic relationships indicates why and how two separated sedimentary packages were tectonically amalgamated. Within this chapter, the geometries and kinematics of 3 representative structural domains can illustrate the style and nature of the deformation in the study area.

3.1 Structural boundaries

As mentioned in the Section 2.2, the North Shuangbaotang Complex is bounded by two major faults along the northern and southern margin. In addition, package 1 is in fault contact with package 2 within the North Shuangbaotang Complex. The beginning of the structural analysis in this session is identifying and deciphering the nature of the 3 major fault contacts: Northern fault, Southern fault and Internal fault (Fig. 3-1).

3.1.1 Nature of the Northern fault

The Northern fault is defined by a northward dipping fault plane, along which the Ordovician to Silurian quartz-rich schist of the Huaniushan Group have moved over the Permian turbidite of the cover package. The older metamorphic basement structurally overlies the younger sedimentary rocks, suggesting that the fault contact in between is a thrust (Fig. 3-2a). A local shear zone is developed along this Northern fault and strikes E-W. This shear zone is characterized by foliations of quartz-rich schist and a fault gouge of turbiditic sandstone. The Permian turbidite beds of the cover package are steeply dipping towards the north and characterized by brittle deformation evidenced by formation of fault gouge near the contact (Fig. 3-2b). In the hanging wall of the shear zone, the Ordovician to Silurian quartz-rich schist of the Huaniusan Group is strongly foliated and dips toward the north (Fig. 3-2c). The juxtaposition of different styles of deformation and rocks of different metamorphic grade on

either side of the shear zone indicate that the root of the shear zone initially developed relatively deep in the ductile realm and the hanging wall rocks were subsequently transported to a shallower level where deformation became brittle over time. Both the presence of older and higher-grade rocks in the hanging wall of the fault over a long strike length indicates it must have accommodated a significant component of reverse motion.

3.1.2 Nature of the Southern fault

The Southern fault separates the Liuyuan Complex from the Ordovician to Silurian metamorphic basement of another segment of the Huaniushan Group and Permian sedimentary rocks (Fig. 3-1). The Southern fault in the southwestern part of the study area is defined by northwestward dipping foliation of quartz-rich schist of the Huaniushan Group structurally overlying the Permian Liuyuan Complex. Unfortunately, the fault contact between the Liuyuan Complex and the Permian sedimentary rocks in the southeastern part of the study area is not exposed. The Southwest-Northeast striking Southern fault contact is inferred to extend continuously northeastward and also represents the contact between the Liuyuan Complex and the Permian sedimentary rocks (Fig. 3-1). The southern fault also probably accommodated a major component of reverse motion, based on the same geological arguments as presented for the Northern fault.

3.1.3 **Nature of the Internal fault**

The fault contact between packages 1 and 2 mentioned in Chapter 2 is named the Internal fault in this study (Fig. 3-1). The Internal fault is interpreted as a thrust fault based on two lines of evidence: 1) Older basalt of package 1 structurally overlies younger chaotic sediments of package 2 and 2) shear indicators identified near the contact described below.

The mudstone near the contact between basalt and chaotic sediments was sheared to form a set of paralleled schistosities (S Plane) and cut by the C Plane suggesting the Internal fault moved top to the west (Figs. 3-3a, 3-3b and 3-3c). This Internal fault indicates that the two sedimentary packages were originally exotic to each other and were tectonically juxtaposed later.

3.2 Structural domains

Three major structural domains were identified in the study area (Chapter 2). These domains are underlain by packages 1, 2, ash beds of the volcanic unit and the cover package, respectively. The ash beds and the cover package form subdomains in domain 3. The structural evolution and style of each domain contributes to the understanding of the tectonic evolution of the North Shuangbaotang Complex. The stereonet plots reveal that the structural patterns of structural domain 1 (package 1) is in many respects similar to that of structural domain 2

(package 2). However, the structure of the ash beds and cover package (structural domain 3a and 3b) are different from those in domains 1 and 2.

3.2.1 **Structural domain 1**

Structural domain 1 is underlain by the greywacke of package 1, which is situated in the hinge area of a large E-W trending fold (Figs. 2-1, 3-1). The poles of sandstone beds in structural domain 1 are not concentrated but spread along a great circle defining a π plane (212, 14). The calculated fold axis of structural domain 1 is (120, 76) (Fig. 3-4).

3.2.2 **Structural domain 2**

Structural domain 2 is underlain by package 2 and its outcrop pattern is largely controlled by the same large fold structure that regulates domain 1 (Figs. 2-1, 3-1). The poles to beddings of sandstone and conglomerate define a π plane (207, 27) associated with a steeply plunging fold axis (117, 63) (Fig. 3-4). The orientation of the axial plane of the fold is ca. (110, 71). Most of the beds in structural domain 2 dip towards the east or southeast. The correspondence in the plunge of the large fold that controls the outcrop pattern of both domains 1 and 2, shows it represents a steeply east plunging (63-76^{o}), E-W trending steeply inclined antiform, which is folding the internal fault between packages 1 and 2 and the unconformity (Fig. 3-1).

Hence, structural domains 1 and 2 were probably subjected to two phases of deformation (D_1 and D_2), because the unconformity, folded internal fault and steeply plunging fold axes suggests that the beds that define the antiform were already faulted and tilted into a steeply dipping orientations by an earlier deformation (D_1) before large-scale F_2 folding.

3.2.3 **Structural domain 3**

Structural domain 3 is subdivided into two subdomains: 3a, underlain by the rhyolite porphyry, ash beds and interlayered siltstone, and 3b, underlain by the cover package. Both subdomains are grouped together into one domain, because they both show no evidence for significant D_1 tilting prior to F_2 folding and display a very similar D_2 structural history, despite the presence of an unconformity between them. A detailed description and interpretation of two deformation phases are presented in Section 5.3.

The Permian cover package is folded by the F_2 antiform that deforms domains 1 and 2 and a large east-plunging synform, cored by the conglomerate of the cover package, towards the north (Figs. 2-1, 3-1). Both the large antiform and synform pair in the cover package plunge shallowly towards the east (Fig. 3-4). The synform connects the ash beds and the rhyolite porphyry in the immediate footwall of the Northern fault with package 2 in the subsurface. The ash beds are folded into a shallowly east-plunging synform with a fold axis (087, 15) (Fig.3-4) that is parasitic to the F_2 synform in the cover package (Figs. 2-1, 3-1), yet is slightly truncated

by the unconformity at the base of the cover sequence, suggesting pre-D_2 tilting of the ash beds was minor. Structural domain 3b is characterized by a fold-thrust belt style deformation of turbidite and conglomerate, with large-scale folding of ash beds interbedded with siltstone. According to the steronet plot, sedimentary beds of the cover package in structural domain 3b are striking near ca. 070^o and dip steeply either to the southeast or northwest (Fig. 3-4). The poles to beddings of the cover package define a π plane (153, 88) with a shallowly plunging calculated fold axis (063, 2) on the steronet. The field measurements of fold axial plane and fold axis of the turbidite are ca. (083, 80) and (085, 15), respectively, which are consistent with the orientations determined by the steronet plot. Generally, foliations and lineations are not well developed or absent in structural domain 3.

3.2.4 **Summary of structural domains**

By comparing structural pattern of the thee structural domains in the study area, it is noted that packages 1 and 2 share 3 similarities:

1) Their fold axes are steeply plunging with both axes approximately lying in a plane that trends ca. 110º.
2) Most of the beddings are moderately to steeply dipping towards the east.
3) Neither of them developed tectonic foliation or lineations.

However, the structural pattern of the cover package is different and more straightforward, which is characterized by abpproximately E-W trending steeply inclined folds with shallowly eastward plunging fold axes, which indicates the cover package only records the last phase of deformation (D_2).

3.3 Road-cut cross-section

The structure of the turbidites of the cover package is well preserved and solely recorded D_2 deformation. A 144 m-long road-cut cross-section of turbidite illustrates well the structural style of the cover package. This road-cut cross-section comprises three representative domains: Domain A, Domain B and Domain C, which are separated by faults (Fig. 3-9).

3.3.1 Domain A

Domain A consists of sandstone beds interbedded with siltstone, which is deformed into a series of mainly southeast-dipping thrust faults (Fig. 3-9). The sedimentary beds in the domain are dominantly younging toward the southeast. The northern boundary of domain A is marked by a north-dipping fault. The geometry and bed truncations of the moderately to steeply southeast-dipping thrust faults indicate a northwest-directed structural transport direction. Duplex structures have been identified, whereas a horse is created where a higher thrust fault

cuts a lower thrust fault (Fig. 3-5 and Fig. 3-9). The fault truncations are best recorded and preserved in the sandstone layers due to their higher competency.

3.3.2 **Domain B**

Bedding of turbidite in domain B is generally dipping towards the southeast. Layering of turbidite is more coherent in domain B showing fewer fault truncations than in domain A. Overall, beds are younging towards the southeast. However, a few beds are locally overturned and younging northwards. A reverse fault with top to the southeast kinematics at a high angle to bedding was identified within domain B. This top to southeast movement is evidenced by the deflection of the sandstone layer (Fig. 3-6 and Fig. 3-9). Sandstone layers in domain B are also boudinaged due to their higher competence suggesting top to the northwest shear sense (Fig. 3-7). Faulting mainly comprises southeast-dipping reverse or thrust faults that moved to the northwest.

3.3.3 **Domain C**

Domain C is characterized by an NW-directed, steeply SE-dipping thrust fault that truncates the southern limb of an upright fold (Fig. 3-8). Folds within domain C vary in shape and interlimb angle. The folds of domain C gradually become more open and upright toward the NW, suggesting the tightness of the folds is due to strain localization associated with the

formation of the thrusts. The orientations of the major fold axis and fold axial plane are (070, 07) and (245, 78) respectively. It is noted that the orientation of folds in domain C are consistent with the general orientation of the folding structures in cover package (Fig. 3-4).

3.3.4 **Summary of the road-cut cross-section**

The structures in the described road-cut cross-section generally represent the structural style of the whole Permian cover package, which is characterized by fold-thrust belt style of deformation. The overall kinematics of thrusting in the cover package is top to the NW. A few reverse faults with top to the SE movement in the road-cut cross-section indicates that back thrusting probably occurred simultaneously with main thrusting.

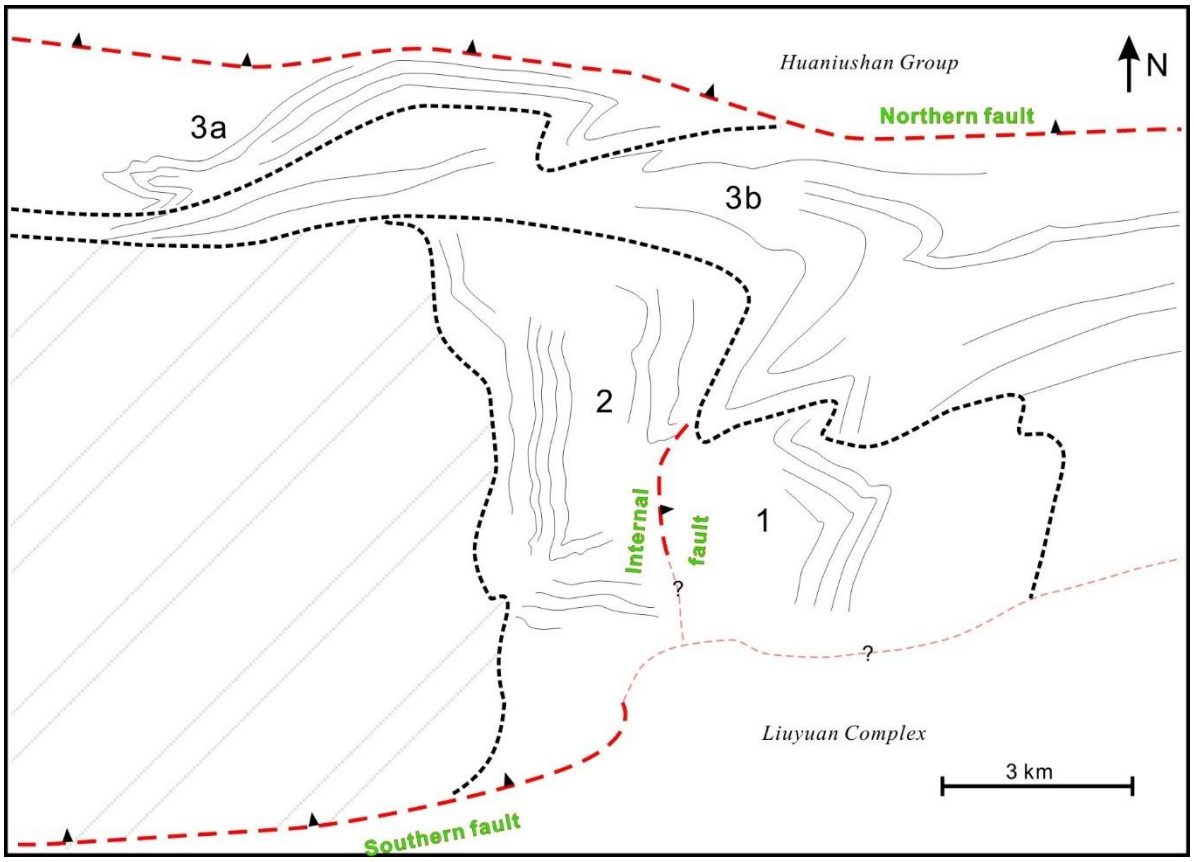

Figure 3-1 Structural map of the study area showing the structural domains and their structural boundaries. The North Shunagbaotang Complex in the middle is sandwiched by Northern fault and Southern fault. Black dash lines are unconformities. Red dash lines are fault contacts. The pale red dash lines are inferred fault contacts covered by sediments.

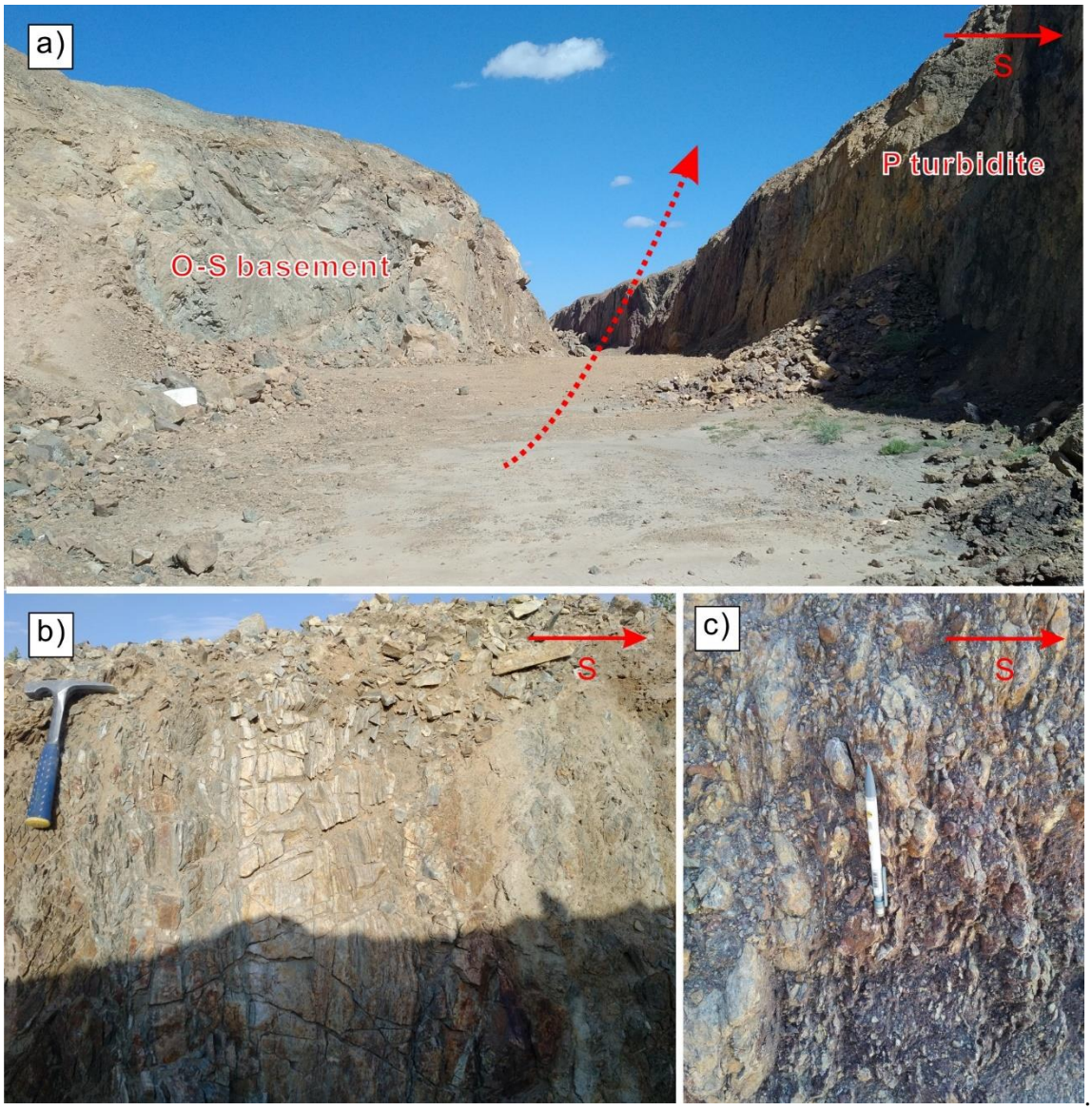

Figure 3-2 Photos of outcrops showing the deformations of the Northern fault boundary. a) Photo of the outcrop showing the O-S basement thrust southward to the top of the Permian cover package. b) Photo of the metamorphic basement developed along the Northern fault boundary showing steep foliations. c) Photo of fault gouge derived from brittlely deformed cover package.

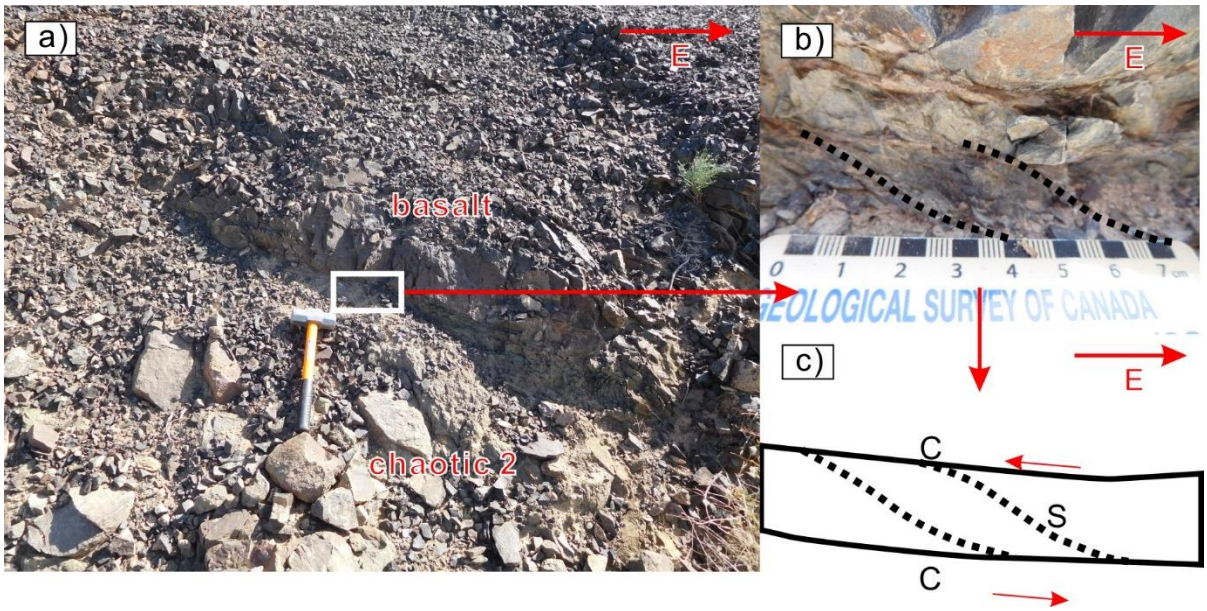

Figure 3-3 Photos and sketch of the Internal fault boundary. a) Photo of outcrop showing the basalt of the package 1 thrust to the top of the chaotic 2. b) and c) Photo and sketch of S-C fabrics showing top to west shear sense.

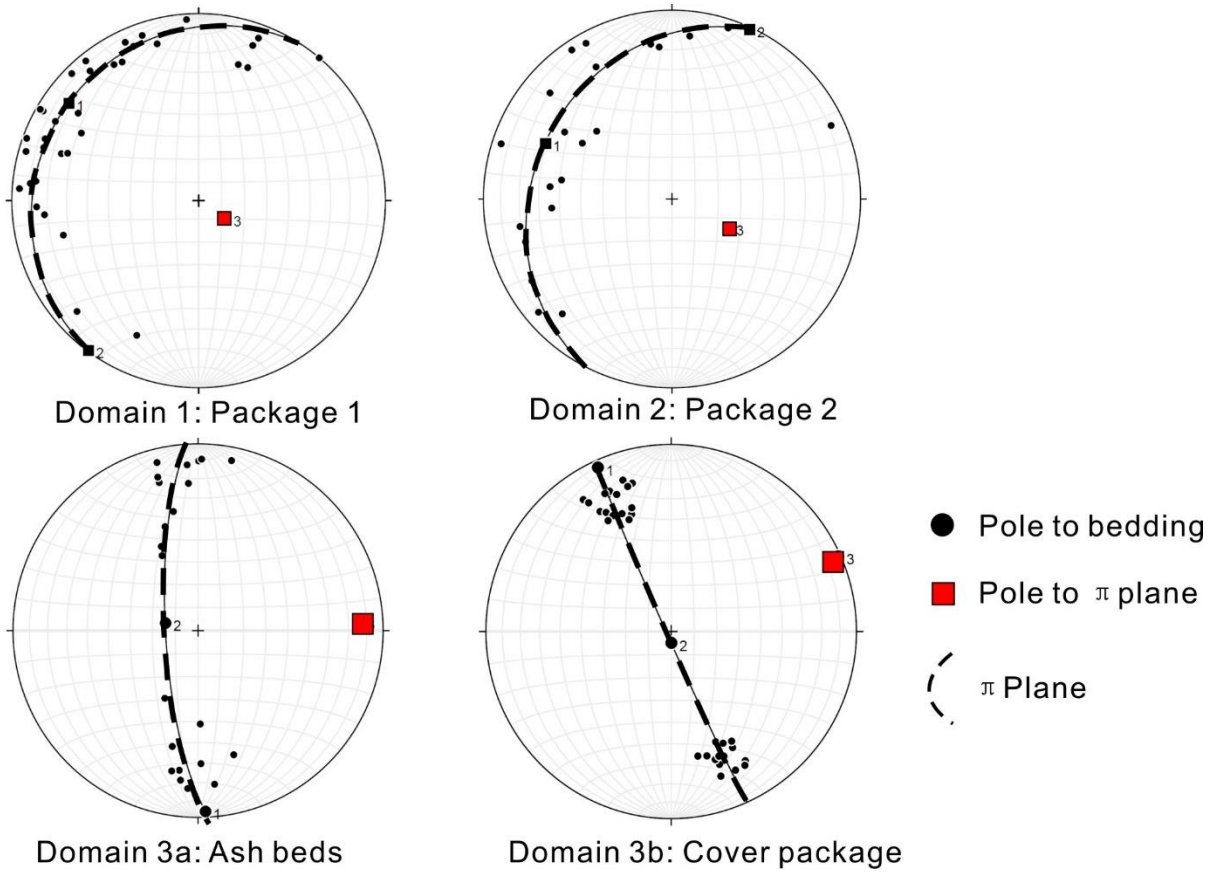

Figure 3-4 Equal area steronets for three structural domains in the study area showing their structural patterns. Structural domain 1, 2, 3a and 3b are represented by package 1, 2, ash beds and cover package, respectively.

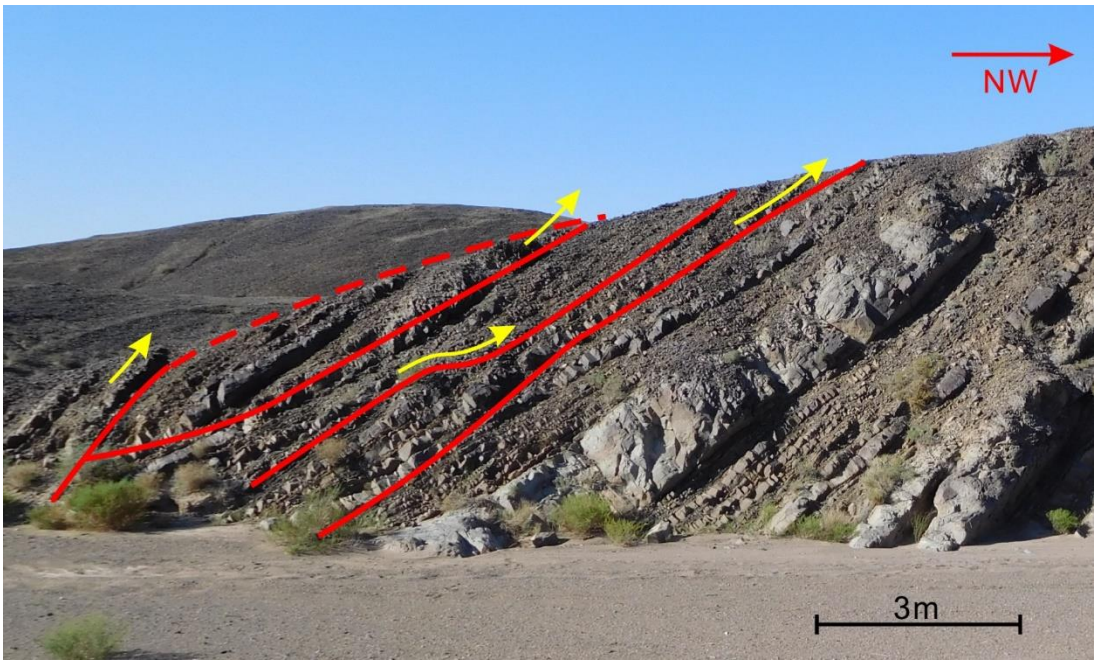

Figure 3-5 Photo of domain A in road-cut cross-section showing cross cutting relationship. The lower thrust fault cut higher thrust fault showing top to NW kinematics.

Figure 3-6 Photo of outcrop showing a reverse fault in domain B.

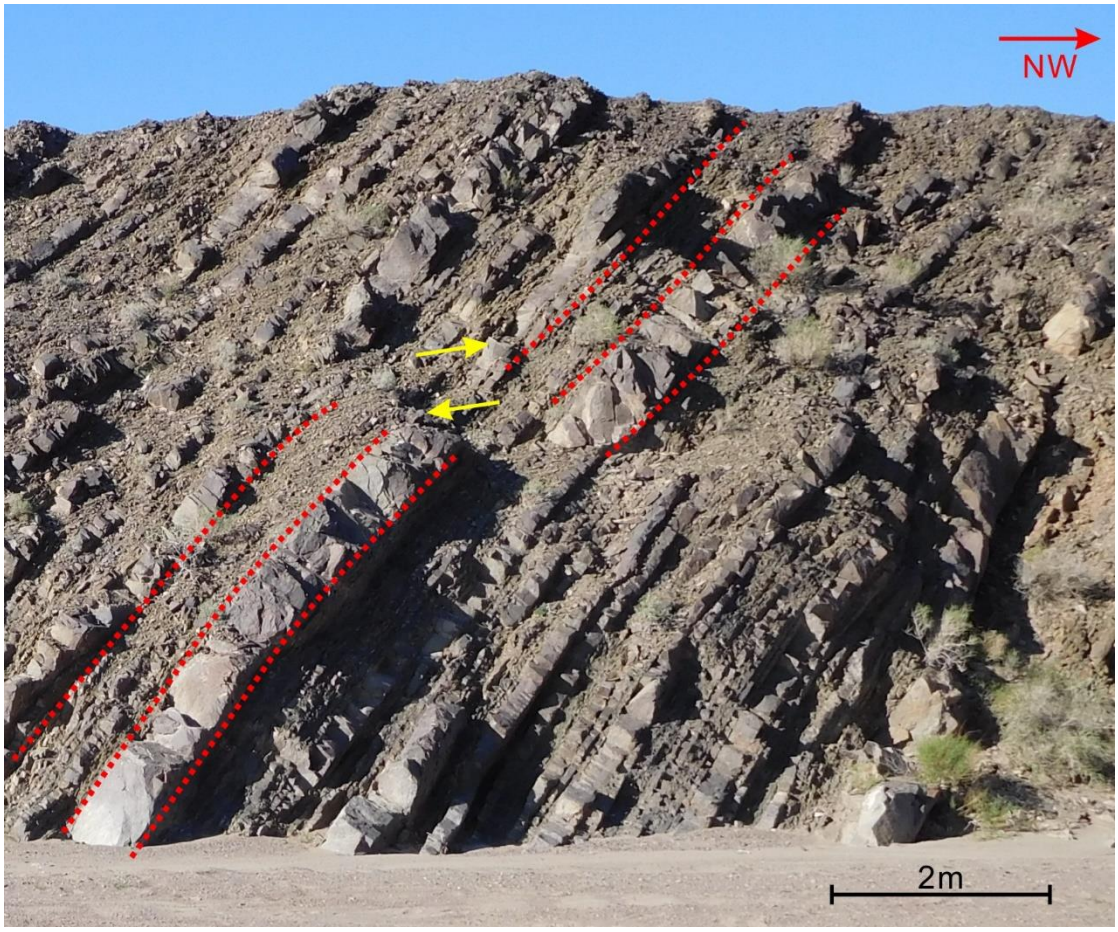

Figure 3-7 Photo of domain B showing boudinage of sandstone layer.

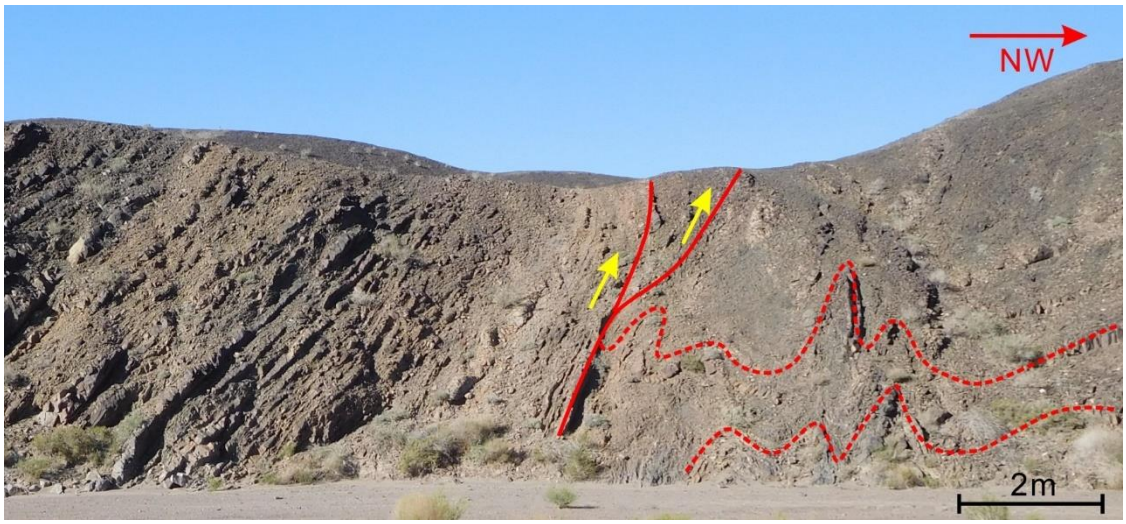

Figure 3-8 Photo of domain C in cross section. A top to NW thrust fault truncates the southern limb of the fold.

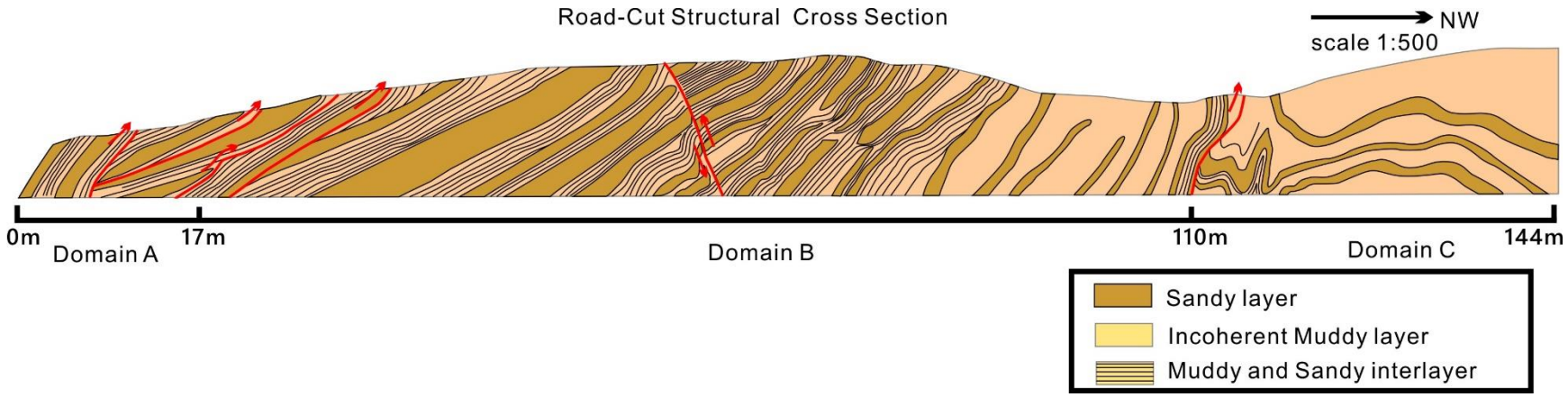

Figure 3-9 A 144 m long road-cut structural cross section of turbidite in the cover package. Three domains are identified in this cross section. The vertical and horizontal scales are identical.

Chapter 4. Geochronological constraints

4.1 Introduction

The relative ages of different sedimentary rocks within the study area generally can be constrained by the younging indicators. However, their absolute ages rely on fossils and geochronology. Within this study, four igneous zircon samples were collected for SHRIMP U-Pb isotopic dating. They include: 1) sample 16-LYJ-119A, a rhyolite porphyry, sampled from the volcanic unit in the northern part of the study area, 2) sample 16-LYJ-182, from an ash bed in the northwestern part of the study area, 3) sample 17-LYJ-2091A, a rhyolite boulder in the chaotic sediments of the package 2, and 4) sample 16-LYJ-60B, a trondhjemite intrusion of the Liuyuan Complex. The locations of the dated samples are marked by a star in Fig. 2-1.

4.2 Analytical technique

The first step of the geochronological analysis is zircon separation, which was conducted at the Langfang Rock-mineral Preparation Laboratory of Hebei Geological Survey Bureau, China. Rock samples were crushed and sorted by electromagnetic separation and heavy liquid separation to obtain the main population of zircon grains (Hu et al., 2013). Selected zircon grains then were sent to the Beijing SHRIMP Center.

The U-Th-Pb isotopic composition of 4 samples in this study were analyzed by sensitive high-resolution ion microprobe (SHRIMP) at Beijing SHRIMP Center, Chinese Academy of

Geological Sciences. Selected zircon grains from the samples were mounted and polished together with a standard zircon (TEMORA) before the SHRIMP analysis. The standard zircon TEMORA (416.8 MA) were used for inter-element fraction. The cathodoluminescence (CL) photography of morphology and internal structure of zircon grains guided the spot selection during the final SHRIMP analysis. The final data processing was carried out by Isoplot and SQUID written by Ludwig. The concordant ages quoted in the text are $^{206}Pb/^{238}U$ ages, which are the weighted mean at the 95% confidence level.

4.3 Results of selected samples

Sample 16-LYJ-119A is a porphyritic rhyolite with phenocrysts of quartz and feldspar (Fig. 4-1). This sample is located in the northwestern part of the study area (Fig. 2-1). The igneous zircons picked from the rhyolite yielded good prismatic crystal shapes with aspect ratios ranging from 1 to 3. The internal texture of zircon is characterized by oscillatory zoning according to the CL image (Fig. 4-2). 13 of 15 analyzed zircon grains fit the concordance criteria. The weight mean Concordia U-Pb age of the rhyolite is 282.2 ± 2.1 Ma with a MSWD value of 2.2(Fig. 4-3 and Table 4-1).

Sample 16-LYJ-182 was collected from the ash beds (Fig. 4-1). The ash beds are interbedded with siltstone in the western part of the cover package (Fig. 2-1). Zircons picked from the ash beds yielded sub-regular prismatic crystal shapes (Fig. 4-2). 4 zircon grains were excluded because of high Uranium concentration. 11 zircon grains fit concordance criteria and

yield two concordant U-Pb ages of 281.9 ± 2.2 Ma and ca. 440 Ma with a MSWD value of 1.04 (Fig. 4-3 and Table 4-2). The younger age is identical to the age of rhyolite within error. The older age is probably inherited from older magmatic rocks located at depth (Cleven et al., 2017).

Sample 17-LYJ-2091A is a porphyritic rhyolite boulder from the chaotic sediments of package 2 (Figs. 2-1 and 4-1). Zircon grains appear to be euhedral with oscillatory zooning (Fig. 4-2). In total, 14 analyzed zircons fit the concordance criteria. The weight mean concordant U-Pb age of the rhyolite boulder is 279 ± 1.6 Ma with a MSWD value of 1.14 (Fig. 4-3 and Table 4-3). The zircons from both the rhyolite boulder and the rhyolite porphyry have similar morphologies and overlap in age within error.

Sample 16-LYJ-60B is a trondhjemite dike from the Liuyuan Complex in the southern part of the study area (Figs. 2-1 and 4-1). Analyzed zircon grains have euhedral shapes and oscillatory zoning (Fig. 4-2). 13 of 15 analyzed zircon grains fit the concordance criteria. The weight mean concordant age of trondhjemite is 285 ± 2.5 Ma with a MSDW value of 1.01 (Fig.4-3 and Table 4-4).

In addition, the youngest population of the detrital zircon ages of the turbidite of the cover package is ca. 277 Ma (Cleven et al., 2017). Therefore, the volcanic unit is a probable provenance of the turbidite of package 2 as well. The older age population of 432 Ma is identical to the inherited age of sample 16-LYJ-182 within error (Fig. 4-3).

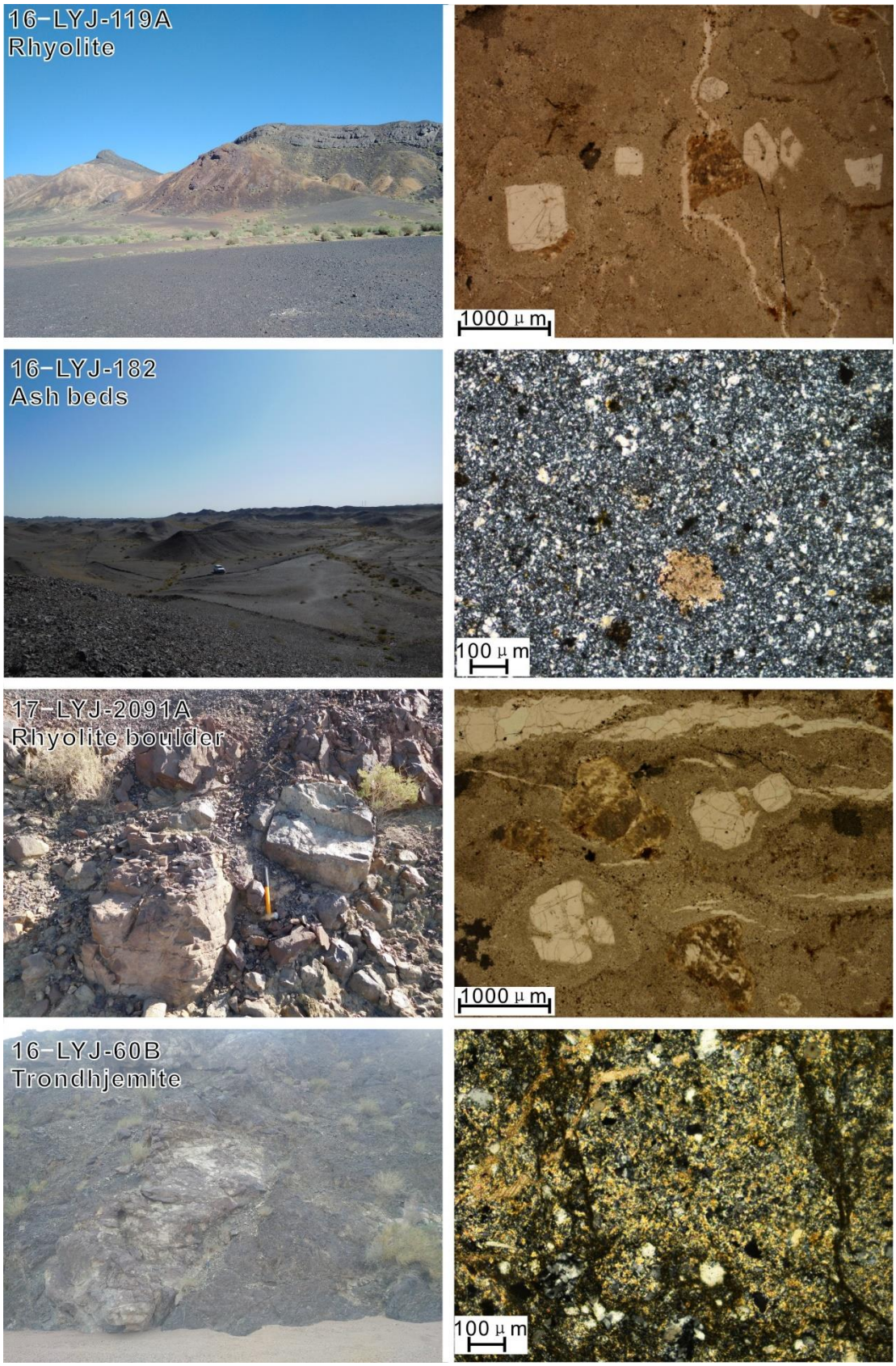
16-LYJ-119A
Rhyolite
1000 μm
16-LYJ-182
Ash beds
100 μm
17-LYJ-2091A
Rhyolite boulder
1000 μm
16-LYJ-60B
Trondhjemite
100 μm

Figure 4-1 Photos of outcrop and thin sections for selected geochronological samples.

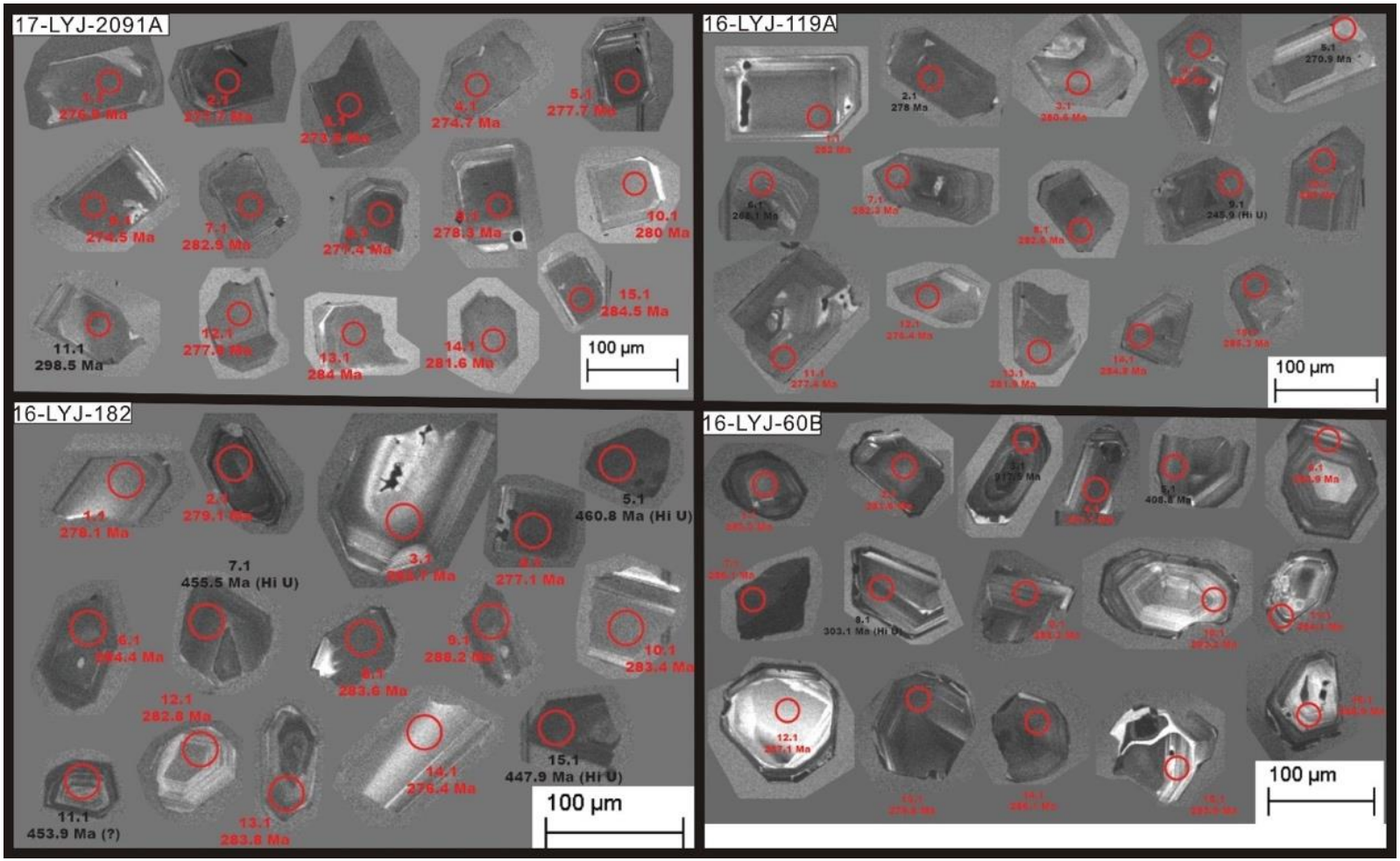

Figure 4-2 CL images for geochronological samples in study area.

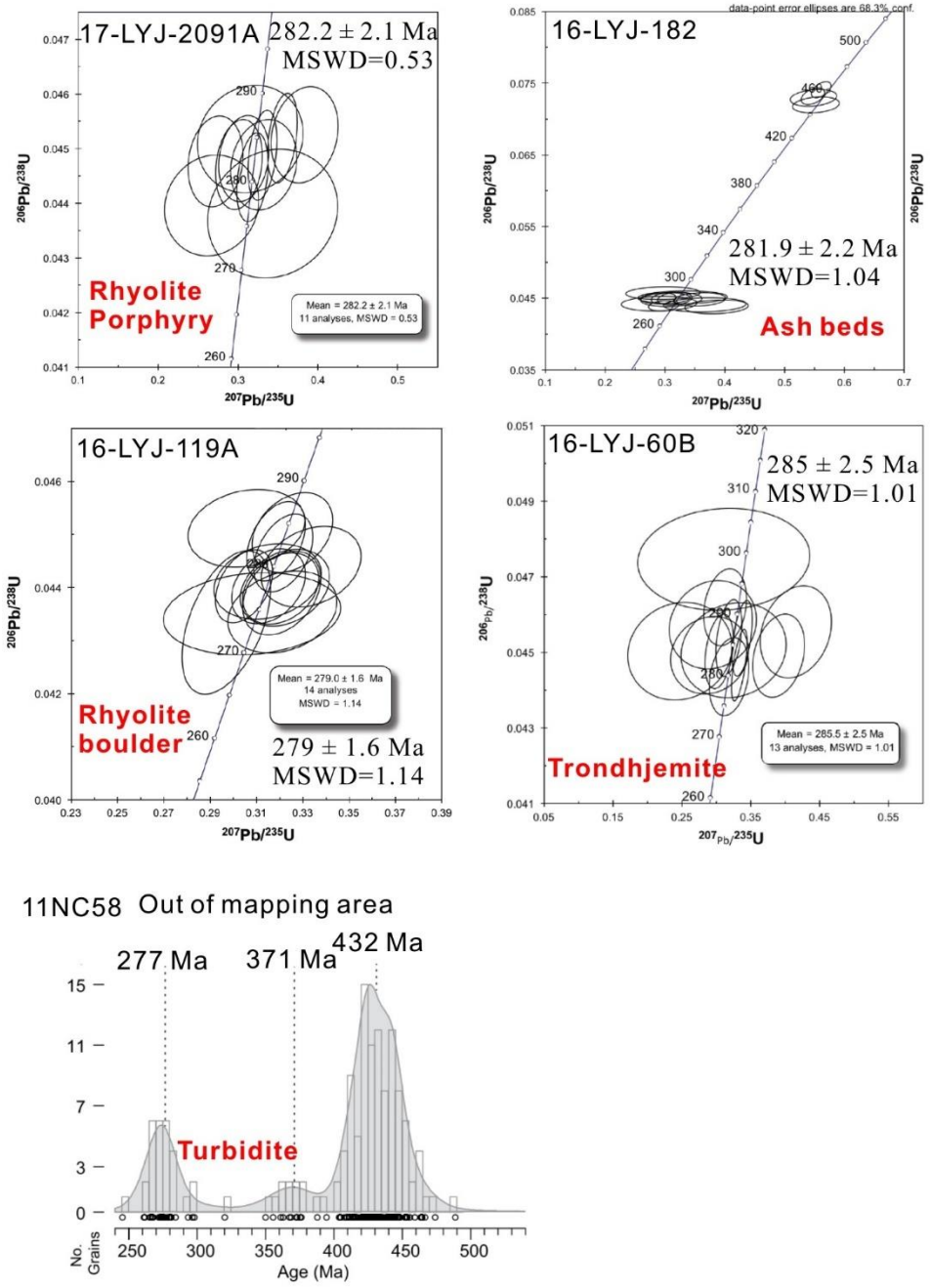

Figure 4-3 Concordia diagrams for analyzed geochronological samples in this study. Sample 11NC58 is from Cleven et. al. (2018).

Table 4-1 SHRIMP U-Pb analysis for the rhyolite porphyry (Sample 16-LYJ-119A). Errors are 1-sigma; Pb_c and Pb* indicate the common and radiogenic portions, respectively. Error in Standard calibration was 0.23% (not included in above errors but required when comparing data from different mounts). (1) Common Pb corrected using measured ^{204}Pb. (2) Common Pb corrected by assuming $^{206}Pb/^{238}U$-$^{207}Pb/^{235}U$ age-concordance. (3) Common Pb corrected by assuming $^{206}Pb/^{238}U$-$^{208}Pb/^{232}Th$ age-concordance.

Spot	$^{206}Pb_c$ (ppm)	U (ppm)	Th (ppm)	$^{232}Th/^{238}U$	$^{206}Pb^*$ (ppm)	Age			Isotopic ratio					
						$^{206}Pb/^{238}U$	$^{207}Pb/^{206}Pb$	$^{208}Pb/^{232}Th$	$^{207}Pb^*/^{206}Pb^*$	±%	$^{207}Pb^*/^{235}U$	±%	$^{206}Pb^*/^{238}U$	±%
1.1	0.51	383	283	0.76	14.8	282.0 ± 3.4	142 ± 150	271 ± 10	0.0489	6.3	0.301	6.4	0.04471	1.2
2.1	15.32	654	649	1.02	29.3	278.6 ± 4.6	-1,700 ±2900	237 ± 37	0.025	84	0.15	84	0.04416	1.7
5.1	40.72	315	276	0.90	19.6	273 ±12	250 ±1700	204 ±140	0.051	72	0.31	72	0.0433	4.4
3.1	--	372	210	0.58	14.2	280.5 ± 3.3	279 ± 88	300.1 ± 7.1	0.0519	3.9	0.318	4.0	0.04448	1.2
4.1	--	348	205	0.61	13.5	285.0 ± 3.3	493 ± 70	292.4 ± 7.4	0.0571	3.2	0.356	3.4	0.04520	1.2
6.1	12.20	384	350	0.94	16.0	268.6 ± 5.8	-100 ±1100	155 ± 43	0.044	46	0.26	46	0.04254	2.2
8.1	1.54	502	327	0.67	19.6	282.7 ± 3.2	181 ± 150	272 ± 12	0.0497	6.6	0.307	6.7	0.04483	1.2
7.1	1.72	433	276	0.66	16.9	282.4 ± 3.4	-109 ± 200	243 ± 13	0.0440	8.3	0.272	8.4	0.04478	1.2
9.1	17.68	747	678	0.94	30.3	246.6 ± 4.5	-430 ±1500	239 ± 41	0.039	58	0.21	58	0.03900	1.8
10.1	0.20	376	206	0.57	14.5	283.0 ± 3.4	347 ± 78	280 ± 11	0.0534	3.4	0.331	3.6	0.04488	1.2
11.1	2.88	393	304	0.80	15.3	277.4 ± 3.8	-108 ± 360	260 ± 19	0.0440	15	0.267	15	0.04398	1.4
12.1	0.39	259	173	0.69	9.79	276.4 ± 4.8	486 ± 340	283 ± 29	0.0568	16	0.343	16	0.04381	1.8
13.1	--	367	203	0.57	14.1	281.9 ± 3.4	367 ± 180	287.9 ± 9.7	0.0539	8.1	0.332	8.2	0.04470	1.2
14.1	--	365	198	0.56	14.0	285.3 ± 3.6	654 ± 150	325 ± 17	0.0614	7.1	0.383	7.2	0.04525	1.3
15.1	3.30	358	271	0.78	14.4	285.0 ± 4.0	222 ± 320	260 ± 21	0.0506	14	0.315	14	0.04519	1.4

Table 4-2 SHRIMP U-Pb analysis for the ash beds (Sample 16-LYJ-182). Errors are 1-sigma; Pb_c and Pb* indicate the common and radiogenic portions, respectively. Error in Standard calibration was 0.23% (not included in above errors but required when comparing data from different mounts). (1) Common Pb corrected using measured ^{204}Pb. (2) Common Pb corrected by assuming $^{206}Pb/^{238}U$-$^{207}Pb/^{235}U$ age-concordance. (3) Common Pb corrected by assuming $^{206}Pb/^{238}U$-$^{208}Pb/^{232}Th$ age-concordance.

Spot	$^{206}Pb_c$ (ppm)	U (ppm)	Th (ppm)	$^{232}Th/^{238}U$	$^{206}Pb^*$ (ppm)	Age $^{206}Pb/^{238}U$		Age $^{207}Pb/^{206}Pb$		Age $^{208}Pb/^{232}Th$		Isotopic ratio $^{207}Pb^*/^{206}Pb^*$	±%	Isotopic ratio $^{207}Pb^*/^{235}U$	±%	Isotopic ratio $^{206}Pb^*/^{238}U$	±%
1.1	2.00	269	372	1.43	10.4	278.1	±4.0	614	±270	290	±12	0.0603	12	0.367	12	0.04409	1.5
2.1	6.24	857	397	0.48	34.8	279.1	±4.2	82	±340	246	±39	0.0476	14	0.291	14	0.04424	1.6
3.1	0.90	235	179	0.79	9.12	282.7	±4.0	206	±250	261	±18	0.0502	11	0.311	11	0.04484	1.4
4.1	0.87	532	463	0.90	20.2	277.1	±3.0	158	±130	265.9	± 7.3	0.0492	5.5	0.298	5.6	0.04392	1.1
5.1	0.23	1006	257	0.26	64.2	460.8	±4.5	410	± 37	421	±12	0.05493	1.6	0.561	1.9	0.07409	1.0
8.1	0.66	507	943	1.92	19.7	283.6	±3.0	100	±100	271.6	± 4.4	0.0480	4.4	0.298	4.5	0.04498	1.1
6.1	9.08	680	451	0.69	29.0	284.4	±3.7	327	±340	253	±34	0.0530	15	0.329	15	0.04511	1.3
7.1	0.26	904	543	0.62	57.0	455.5	±4.6	380	± 49	452.1	± 8.4	0.0542	2.2	0.547	2.4	0.07321	1.0
9.1	2.29	555	209	0.39	22.3	288.2	±3.6	52	±330	222	±39	0.0470	14	0.297	14	0.04572	1.3
10.1	0.61	392	524	1.38	15.2	283.4	±3.7	243	±130	273.1	± 8.5	0.0510	5.8	0.316	5.9	0.04494	1.3
11.1	0.67	506	276	0.56	31.9	453.9	±4.6	393	±100	436	±16	0.0545	4.5	0.549	4.7	0.07296	1.1
14.1	0.60	145	152	1.08	5.51	276.4	±4.0	740	±190	286.5	± 9.2	0.0640	9.0	0.386	9.1	0.04381	1.5
12.1	0.37	199	105	0.55	7.69	282.8	±3.8	524	±170	301	±21	0.0578	7.9	0.358	8.0	0.04485	1.4
13.1	1.07	521	224	0.44	20.4	283.8	±3.2	119	±210	265	±19	0.0484	9.1	0.300	9.2	0.04500	1.2
15.1	2.62	1481	597	0.42	94.0	447.9	±4.4	440	±100	423	±27	0.0557	4.6	0.553	4.7	0.07196	1.0

Table 4-3 SHRIMP U-Pb analysis for the rhyolite porphyry boulder in package 2 (Sample 17-LYJ-20191A). Errors are 1-sigma; Pb_c and Pb* indicate the common and radiogenic portions, respectively. Error in Standard calibration was 0.23% (not included in above errors but required when comparing data from different mounts). (1) Common Pb corrected using measured ^{204}Pb. (2) Common Pb corrected by assuming $^{206}Pb/^{238}U$-$^{207}Pb/^{235}U$ age-concordance. (3) Common Pb corrected by assuming $^{206}Pb/^{238}U$-$^{208}Pb/^{232}Th$ age-concordance.

						Age			Isotopic ratio					
Spot	$^{206}Pb_c$ (ppm)	U (ppm)	Th (ppm)	$^{232}Th/^{238}U$	$^{206}Pb^*$ (ppm)	$^{206}Pb/^{238}U$	$^{207}Pb/^{206}Pb$	$^{208}Pb/^{232}Th$	$^{207}Pb^*/^{206}Pb^*$	±%	$^{207}Pb^*/^{235}U$	±%	$^{206}Pb^*/^{238}U$	±%
1.1	--	283	176	0.64	10.7	276.9 ±3.2	330 ± 74	271.4 ± 6.6	0.0530	3.2	0.321	3.5	0.04390	1.2
2.1	0.16	696	422	0.63	26.4	277.7 ±2.8	203 ± 57	269.7 ± 5.4	0.0502	2.5	0.3045	2.7	0.04402	1.0
3.1	0.49	521	296	0.59	19.5	273.5 ±5.5	180 ± 87	261.4 ± 9.0	0.0497	3.7	0.297	4.3	0.04334	2.1
4.1	0.33	333	222	0.69	12.5	274.7 ±3.2	350 ±110	272.4 ± 8.8	0.0535	4.7	0.321	4.8	0.04354	1.2
5.1	0.43	537	369	0.71	20.4	277.7 ±2.9	282 ± 72	265.6 ± 8.5	0.0519	3.2	0.315	3.3	0.04403	1.1
6.1	0.46	541	323	0.62	20.3	274.5 ±3.2	257 ±190	267 ±16	0.0514	8.1	0.308	8.2	0.04350	1.2
7.1	0.00	360	238	0.68	13.9	282.9 ±3.1	262 ± 54	289.4 ± 5.9	0.0515	2.4	0.3185	2.6	0.04487	1.1
8.1	0.50	950	646	0.70	36.1	277.4 ±2.7	322 ± 73	264.1 ± 6.2	0.0529	3.2	0.320	3.4	0.04398	1.0
9.1	0.46	598	432	0.75	22.8	278.3 ±2.9	274 ±110	261.8 ± 8.2	0.0517	4.7	0.315	4.8	0.04411	1.1
10.1	--	365	242	0.69	13.8	280.0 ±3.1	392 ± 92	288.0 ± 8.7	0.0545	4.1	0.334	4.3	0.04439	1.1
11.1	0.37	395	245	0.64	16.1	298.5 ±3.2	254 ± 96	278.9 ± 9.8	0.0513	4.2	0.335	4.3	0.04739	1.1
12.1	0.10	450	290	0.67	17.0	277.6 ±2.9	334 ± 86	265.8 ± 7.0	0.0531	3.8	0.322	3.9	0.04400	1.1
13.1	0.26	405	243	0.62	15.7	284.0 ±3.0	304 ± 76	282.8 ± 7.5	0.0524	3.3	0.325	3.5	0.04504	1.1
14.1	0.75	485	320	0.68	18.9	284.5 ±3.0	154 ±120	258.4 ± 9.6	0.0491	5.3	0.306	5.4	0.04512	1.1
15.1	--	399	293	0.76	15.3	281.6 ±3.0	295 ± 54	270.6 ± 5.4	0.0522	2.4	0.3216	2.6	0.04465	1.1

Table 4-4 SHRIMP U-Pb analysis for the trondhjemite (Sample 16-LYJ-60B). Errors are 1-sigma; Pb_c and Pb* indicate the common and radiogenic portions, respectively. Error in Standard calibration was 0.23% (not included in above errors but required when comparing data from different mounts). (1) Common Pb corrected using measured ^{204}Pb. (2) Common Pb corrected by assuming $^{206}Pb/^{238}U$-$^{207}Pb/^{235}U$ age-concordance. (3) Common Pb corrected by assuming $^{206}Pb/^{238}U$-$^{208}Pb/^{232}Th$ age-concordance.

						Age			Isotopic ratio					
Spot	$^{206}Pb_c$ (ppm)	U (ppm)	Th (ppm)	$^{232}Th/^{238}U$	$^{206}Pb^*$ (ppm)	$^{206}Pb/^{238}U$	$^{207}Pb/^{206}Pb$	$^{208}Pb/^{232}Th$	$^{207}Pb^*/^{206}Pb^*$	±%	$^{207}Pb^*/^{235}U$	±%	$^{206}Pb^*/^{238}U$	±%
1.1	--	325	191	0.61	12.5	283.3 ± 4.2	43 ±300	289.8 ± 8.4	0.0469	13	0.290	13	0.04492	1.5
2.1	--	667	917	1.42	25.6	281.6 ± 3.9	375 ± 38	271.2 ± 4.6	0.05410	1.7	0.3331	2.2	0.04466	1.4
3.1	0.83	696	168	0.25	92.2	917 ±12	855 ± 36	747 ±40	0.0676	1.7	1.424	2.2	0.1529	1.4
4.1	0.33	590	515	0.90	23.5	291.1 ± 4.1	152 ±150	277.5 ± 9.5	0.0491	6.4	0.313	6.6	0.04620	1.4
4.1	0.16	305	154	0.52	17.2	408.8 ± 6.0	372 ±130	392 ±23	0.0540	5.7	0.488	5.9	0.06546	1.5
5.1	0.84	471	375	0.82	18.4	283.9 ± 4.0	146 ± 99	266.2 ± 7.4	0.0490	4.2	0.304	4.5	0.04503	1.5
7.1	0.14	1363	1990	1.51	56.5	303.1 ± 4.2	242 ± 32	285.0 ± 4.5	0.05102	1.4	0.3387	2.0	0.04815	1.4
6.1	0.02	412	202	0.51	16.0	286.1 ± 4.0	367 ± 57	286.8 ± 7.4	0.0539	2.5	0.3372	2.9	0.04538	1.4
8.1	0.94	675	1201	1.84	26.8	288.3 ± 4.8	39 ±340	116.0 ± 7.3	0.0468	14	0.295	14	0.04574	1.7
9.1	--	382	309	0.84	14.7	283.2 ± 4.5	710 ±130	294.2 ± 8.6	0.0630	6.1	0.390	6.3	0.04491	1.6
10.1	1.66	253	148	0.60	9.97	284.2 ± 5.1	299 ±350	279 ±26	0.0523	15	0.325	16	0.04507	1.8
11.1	--	136	90	0.69	5.28	287.1 ± 4.9	812 ±170	329 ±11	0.0662	8.0	0.416	8.2	0.04554	1.8
12.1	0.25	424	335	0.82	16.2	279.8 ± 4.2	289 ±130	271.0 ± 8.1	0.0521	5.8	0.319	6.0	0.04436	1.5
13.1	--	615	686	1.15	24.0	286.1 ± 4.1	233 ± 84	282.8 ± 5.3	0.0508	3.6	0.318	3.9	0.04538	1.5
14.1	3.11	185	119	0.66	7.38	284.0 ± 5.3	-365 ±520	217 ±29	0.0398	20	0.247	20	0.04504	1.9
15.1	2.68	255	165	0.67	10.7	299.0 ± 5.5	72 ±630	322 ±35	0.047	26	0.311	27	0.04747	1.9

Chapter 5. Tectonic interpretations of the stratigraphy and structures

5.1 Introduction

The stratigraphic analysis combined with the structural analysis forms the basis for the following interpretation of the tectonic setting. The stratigraphic analysis is based on the composition, grain size and contact relationships of sedimentary rocks. The structural analysis is based on the structural style and deformational pattern of each sedimentary package. This chapter combines stratigraphic and structural evidence together to constrain the tectonic evolution of a folded Permian imbricated stack in the study area during the final stage of accretionary orogenesis of BOC. The timing of the final stage of accretionary orogenesis thus constrains the timing of the closure of the Paleo-Asian Ocean.

5.2 Interpretation of stratigraphy

5.2.1 Package 1

The sedimentary rocks of package 1 described in Chapter 2 are interpreted to represent trench sediments incorporated in an accretionary wedge. They were mainly derived from mafic rocks of the Liuyuan Complex, and hence, probably formed in an oceanic setting. The basaltic structural basement of package 1 is inferred to form part of the Liuyuan Complex, which is considered a structural slice of a Permian ophiolite accreted to the southern active margin of

Dundunshan terrane during a northward subduction (Mao et al., 2012b). The immediately overlying chaotic sediments of package 1 represent a tectonosome deposit interpreted to have been created by slope failure of a thrust front and characterized by: 1) boudinaged sandstone and pillow basalts in mudstone matrix and 2) chaotic distribution without coherent beds (Pini, 1999). The basaltic composition of the blocks in the tectonosome indicates that it is mainly derived from the material off-scarped from the subducting oceanic plate (Prothero and Schwab, 1996). The mudstone matrix suggests a deep marine sedimentary environment. The tectonic contact between the basaltic basement and structurally overlying tectonosome is consistent with thrusting within an accretionary wedge. The preservation of remnants of an accretionary wedge in the study area indicates that Permian orogenesis was relatively soft, thus parts of the leading edge of the overriding plate were not really removed during exhumation and erosion.

The chaotic sediments are overlain by greywacke, which is also strongly linked to the Liuyuan Complex because it contains basaltic clasts and boulders. The abundance of mafic minerals in the greywacke, such as olivine and pyroxene, confirms a mafic igneous/ volcanic source of the greywacke. In addition, the main feldspar of the greywacke is albite, which is also consistent with a mafic source. The poor sorting and low maturity of the greywacke suggests it was rapidly deposited, close to the source area. The greywacke possibly formed by a submarine avalanche, which transported sediments into trench as submarine turbidite flows.

5.2.2 **Package 2**

The sedimentary rocks of package 2 are mainly derived from Ordovician to Silurian metamorphic basement and associated plutonic rocks, which are completely different from the source of package 1. The different sources are important evidence to separate package 1 and 2 and confirm their tectonic contact based on structural analysis.

The late Carboniferous to early Permian limestone of package 2 (See section 2.3.2) indicates a relatively warm and shallow marine water depositional setting. The deposition of the Carboniferous to Permian limestone requires a tectonically quiescent period. The angular unconformity between the Carboniferous to Permian limestone and overlying sandstone interbedded with conglomerate of package 2 suggests that tectonism had at least started by the early Permian.

The sandstone of package 2 is arkosic because it contains >25% feldspar, which is probably derived from a nearby Ordovician to Silurian pluton. The short transportation distance between the source area and deposition area is consistent with the low maturity of the sandstone and conglomerate of package 2. The red sandstones interbedded with conglomerate are interpreted to represent shallow water deposits, possibly in an alluvial fan setting. The high abundance of feldspar suggests an environment with a relatively low degree of chemical weathering and/or rapid deposition close to the source area. This alluvial fan deposition also

obtained clasts from Permian rhyolite porphyries which may have formed part of a continental arc. If so, package 2 may have been deposited in a forearc basin.

The top stratigraphic level of package 2 is represented by chaotic sediments which are interpreted as a syn-tectonic olistostrome (Pini, 1999). Olistostrome is a sedimentary deposit composed of a chaotic mass of heterogeneous material, such as blocks, sand and mud, formed by submarine gravity sliding (Abbate et al., 1970). The chaotic sediments of package 2 in this study are characterized by chaotic distribution of sandstone blocks, metamorphic blocks and rhyolite boulders in a sandstone matrix which match the definition of olistostrome. The sandstone, metamorphic and rhyolite blocks of the chaotic sediments were probably derived from the underlying stratigraphic units, as a result of tectonically-driven uplift. Syn-tectonic olistostromes were probably associated with thrusts that breached sea level (Pini, 1999).

5.2.3 **Cover package**

The identification of mafic minerals, volcanic clasts and metamorphic lithics in the sedimentary rocks of the cover package suggests a multi-provenance for this unit. The source probably includes the Liuyuan Complex, continental arc and metamorphic basement. The low maturity of the cover package indicates a rapid deposition close to the source area. Sedimentary structures of the cover package rock, such as graded bed, parallel lamination and loading structures, confirm the sedimentary rocks of the cover package were rapidly deposited as

submarine turbidites. An angular unconformity between the cover package and underlying sedimentary rocks is inferred to represent the tectonic uplift-driven erosion of the packages 1 and 2 during the deposition of the cover package. In addition, the grain size of sedimentary rocks is fining upward from the underlying packages 1 and 2 to the overlying turbidite of the cover package suggesting deepening depositional environment caused by the thrust-related tectonic loading. The evidence mentioned above combined with the fold and thrust style of deformation suggests the cover package represent syn-collision foreland basin sediments. Thus, the depositional age of the foreland basin sediments (<ca. 277 Ma in Chapter 4) constrains the timing of final orogenesis to the late Permian.

5.3 Interpretation of structures

The North Shuangbaotang Complex was subjected to at least two phases of deformation (D_1 and D_2). However, the early phase of deformation (D_1) was only recorded in packages 1 and 2 and relatively poorly understood at present. The near E-W trending upright to inclined F_2 folds and associated north-verging thrusts in the cover package represent the main phase of deformation (D_2) in the North Shuangbaotang Complex.

5.3.1 Early deformation (D_1)

The outcrop pattern and the moderate to steep dips of bedding in package 1 and the fault between packages 1 and 2 suggests they are folded by later phase of deformation (D_2) together

with package 2 (Fig. 2-1). The existence of an earlier phase of deformation (D_1) in package 2 is indicated by the steeply southeast-plunging fold axis of F_2 (See Fig. 3-4 in Chapter. 3). The steeply plunging fold axis was probably formed by folding of already tilted beds. There are several structural processes that can produce tilted beds. It may be due to folding, faulting or a combination of both. No evidence for D_1 folding was observed on outcrop scale, but the D_2 -folded fault between package 2 and the structurally overlying basalt of package 1 is moderately to steeply dipping to the east (Fig. 3-4), suggesting D_1 at least involved faulting.

Unfolding the E-W trending upright F_2 fold indicates that the D_1 structures were approximately dipping toward the east or northeast (Fig. 5-1). Combined with the shear indicator of S-C fabrics observed from the D_1-related Internal fault between packages 1 and 2, this suggests a westward thrusting motion (Fig. 3-4), although this could vary anywhere between NW and SW due to the absence of shear-related lineations. According to Fig. 5-1, the original F_1 fold axis is near horizontal, which indicates no earlier deformational phases.

Two lines of evidence suggest D_1 was likely associated with SW-directed thrusting: 1) The southern fault of the North Shuangbaotang Complex is probably a long-lived major reverse fault, presently dipping steeply to the north (See Chapter 3), which is opposite to the generally southerly dip of D_2-related faults in the cover package, suggesting it is a D_2 -steepened D_1 structure; and 2) The subduction was probably to the north according the previous tectonic

models that accommodated incorporation of the Liuyuan Complex into the accretionary wedge (See below) (Xiao et al.,2010a, Mao et al., 2012b).

5.3.2 **Main deformation (D_2)**

The main deformation phase (D_2) of the North Shuangbaotang Complex is represented by E-W trending F_2 folds, particularly the large, steeply east-plunging fold that controls the outcrop pattern of package 2 and underlying basement. The F_2 folds in the cover package are trending E-W and shallowly plunging to the east, suggesting the absence of earlier deformation D_1 in the cover package.

D_2 deformation in the cover package is characterized by north-verging folds and thrusts (See Fig. 3-9 in Chapter. 3), which is inconsistent with the southwest thrusting deduced for D_1. Since D_2 deformation occurred after the deposition of the cover package during the final stage of orogenesis, the thrusting direction of the cover package thus may not be synthetic with the overall subduction polarity.

Windley et al. (2007, p. 43) noted that it is possible to determine the subduction polarity by thrust vergence exclude following situations "1) the back-thrust developed by syn / post-accretionary orogenesis or inherited from the oceanic domain. 2) the overprinting of syn-subduction, accretionary thrusts by later imposed structures." .

5.3.3 **Timing of deformations**

D_1 is represented by imbricated formation of tectonosome in package 1 and formation of syn-tectonic olistostrome in package 2, as a result of folding and/or faulting, tilting of the early Permian sedimentary layers of package 2 into a steeply easterly dipping orientation and juxtaposition of packages 1 and 2 by the Internal fault. Therefore, D_1 had started during the deposition of packages 1 and 2 after the deposition of the Carboniferous to early Permian limestone and to have continued until after ca. 279 Ma, which is the age of the rhyolite porphyry clasts in the olistostrome of package 2. The age of package 1 is younger than ca. 280 Ma if the basalt blocks in package 1 were derived from the Liuyuan Complex; However, they also could be derived from older oceanic crust present in the last vestige of the Paleo-Asian Ocean. The cover package shows no evidence of D_1, D_1 thus is older than the deposition of the cover package (ca. 277 Ma), which is based on the age of the ash beds and the youngest detrital zircon (See Chapter 4). Hence, D_1 probably took place between 280 and 277 Ma, whereas D_2 is younger. However, the evidence for the time of termination of D_2 is lacking, but probably is not much younger than 277 Ma, considering the cover package is interpreted as syn-tectonic foreland basin deposits.

5.4 Tectonic history of this study

Two fault bounded diverse sedimentary packages in the study area were derived from two different terranes. They were structurally juxtaposed during and/or following the Permian closure of the Paleo-Asian Ocean. The last vestiges of the Permian Paleo-Asian Ocean were consumed by the continuous northward subduction of its crust. The final closure of the Paleo-Asian Ocean is represented by the orogenesis associated with accretion of the Dunhuang terrane with the active southern margin of the Dundunshan terrane (Huaniushan Group) (Mao et al., 2012b). The Permian tectonic history of the study area thus can be separated into two stages: 1) stage 1 (D_1) is characterized by a trench - arc system and early collision during the approximately northward subduction of the oceanic crust and docking of the Dunhuang terrane, and 2) stage 2 (D_2) is characterized by the evolution of a retro-foreland basin during continuous collision of the Dundunshan terrane with the Dunhuang terrane and its progressive inversion.

Stage 1 Approximately northward subduction and early collision (before the deposition of the cover package)

The late Carboniferous to early Permian limestone (Guo et al., 2012) suggests that the Paleo-Asian Ocean remained open, at least partly, until the early Permian. Thus, there appears to be a relatively tectonically quiescent period before the onset of Permian tectonism. The angular unconformity between the Carboniferous to Permian limestone and the overlying

sandstone of package 2 indicates the initiation of Permian tectonism, which is consistent with the Permian tectonic model of previous studies (Xiao et al., 2010a; Mao et al., 2012b). The previous tectonic model proposed that the final branch of the Paleo-Asian Ocean was consumed by a double subduction during the Permian (Fig. 1-4) (Xiao et al., 2010a; Mao et al., 2012b). The northward subduction of the oceanic crust formed an accretionary wedge (package 1) and may have reactivated a Permian continental volcanic arc (Fig. 5-2), which is represented by the ca. 282 Ma rhyolite porphyry and ca. 282 ash beds in this study (Fig. 5-2a). Continuous northward subduction tectonically uplifted the Ordovician to Silurian metamorphic basement and plutonic rocks on the upper plate (Dundunshan terrane), probably because of the entrance of the leading edge of the buoyant continental Dunhuang terrane. The sandstone interbedded with conglomerate of package 2 obtained its sediments from the uplifted area, which is interpreted to have been deposited in an alluvial fan setting. Meanwhile, the accretionary wedge (package 1 in this study) and the Liuyuan Ophiolite were thrust southwestward over forearc (package 2) by the Internal fault, which also suggest collision between the Dundunshan terrane and the Dunhuang terrane had started (Fig. 5-2c). Thrusting of accretionary wedge material (package 1) over forearc rocks (package 2) in a northward subduction scenario is most simply explained by southward underthrusting of the accretionary wedge beneath part of the forearc during early collision. Subsequent ‘out-of-sequence’ thrusting emplaced accretionary wedge over forearc basin (Fig. 5-2c).

Stage 2 The evolution of a retro- foreland basin during final stage of orogenesis

Continuous convergence and underthrusting of the buoyant Dunhuang terrane (lower plate) beneath the leading edge of the Dundunshan terrane (upper plate) progressively thickened the collision zone, forming a growing orogenic wedge (Coward, 1994). This in turn, produced uplift and erosion of packages 1 and 2 and other rocks (e.g. Liuyuan Complex) were incorporated into the growing orogenic wedge. North-verging folds and back-thrusts developed in the hinterland of the orogenic wedge, forming a retro-foreland basin mainly built, in part unconformably, upon the previously imbricated rocks of packages 1 and 2 (Fig. 5-2d). Such a model requires that coeval south-directed thrusting and folding took place towards the foreland of the orogenic wedge. D_2 represents the final stage of shortening in this part of the Beishan orogenic collage.

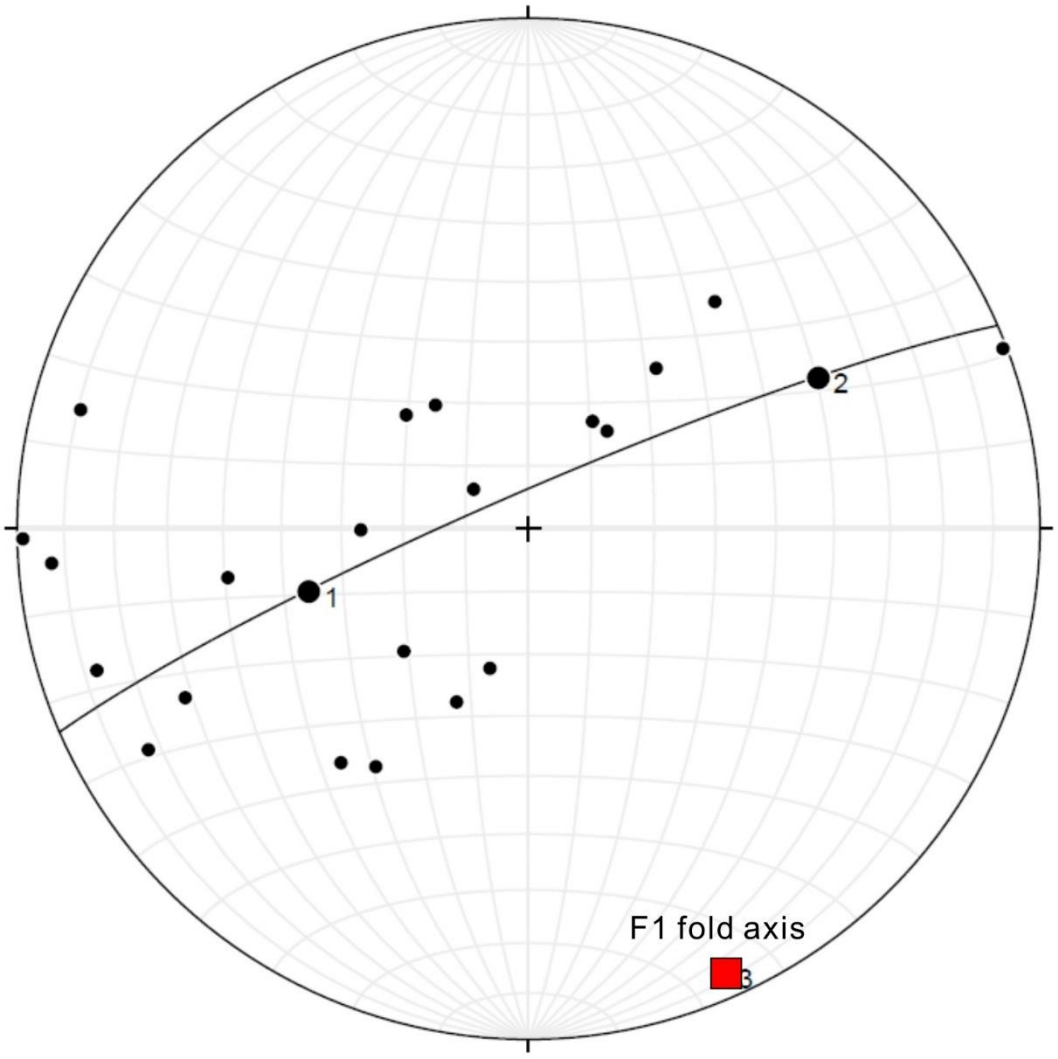

Figure 5-1 Original D_1 structures by unfolding F_2. The F_1 fold axis is near horizontal.

..

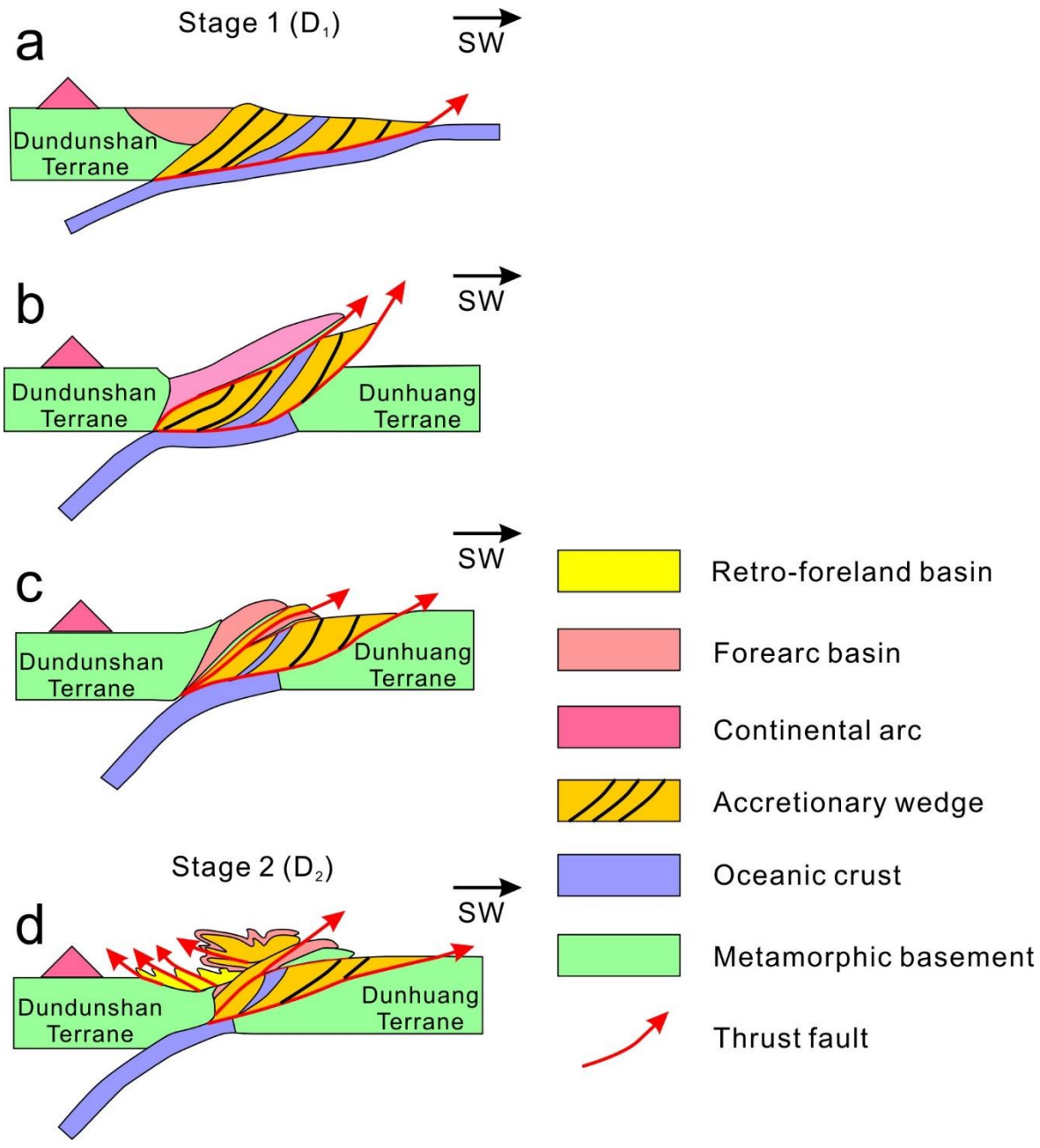

Figure 5-2 Tectonic model proposed in this study. Retro-foreland basin is represented by the cover package; Forearc basin is represented by package 2; Continental arc is represented by rhyolite; Accretionary wedge is represented by package 1.

Chapter 6. Conclusion and Tectonic Implication

The 1:20,000 geological mapping led to a better understanding of the structure and tectono-stratigraphy of the North Shuangbaotang Complex, which is comprised of two diverse, fault-bounded sedimentary packages in turn unconformably overlain by a cover package. The sediment of package 1 is principally derived by erosion and/or mass wasting from the oceanic Liuyuan Complex. The latter is interpreted as a structural slice of ophiolite incorporated into a south-facing accretionary wedge (Fig. 5-2a). The source of the sediments in package 2 is derived from the Ordovician to Silurian metamorphic basement, plutonic rocks and Permian rhyolite porphyries of the Dundunshan terrane and exotic with respect to package 1. The package 1 sediment has an oceanic provenance, indicating these two packages of sedimentary rocks formed in separate tectonic settings. Package 2 is interpreted to have been deposited in a forearc basin built upon the leading edge of the Dundunshuan terrane. The structural juxtaposition between packages 1 and 2 took place during late D_1 by out-of-sequence thrusting emplacing part of the underthrusted accretionary wedge above an allochthonous part of its forearc cover (Fig. 5-2b). The leading edge of the forearc was thrusted earlier during D_1 towards the southwest over the adjacent accretionary wedge, which at this stage included the allochthonous Liuyuan Complex (Fig. 5-2c). The inferred inversion and shortening of the arc-trench gap and out-of-sequence thrusting is related to docking and the early stages of collision between the Dundunshan and the Dunhuang terranes during closure of the last vestige of the

Paleo-Asian Ocean. The fold and fault belt of the cover package unconformably overlying packages 1 and 2 and their fault contact represents the evolution of a retro-foreland basin during the final stage of the orogenesis (Fig. 5-2d). The identification of Permian tectonic elements, such as a small remnant of the accretionary wedge, an allochthonous slice of ophiolite, a part of an inverted forearc basin and associated continental volcanic arc in a complex structural configuration, combined with the presence of a retro-foreland basin with thin-skinned fold and thrust belt style deformation, suggests the Paleo-Asian Ocean was closed in the Permian in this part of the BOC.

A prediction of the tectonic model presented herein is that south-verging structures should have developed in the Dunhuang terrane coeval with the north-verging D_2 structures recognized here. Preliminary structural studies south of the Liuyuan complex support the existence of such structures (van Staal et al., 2018).

Reference

Abbate, E., Bortolotti, V., & Passerini, P. (1970). Olistostromes and olistoliths. Sedimentary Geology, 4(3-4), 521-557.

Allen, M. B., Windley, B. F., & Zhang, C. (1993). Paleozoic collisional tectonics and magmatism of the Chinese Tien Shan, central Asia. *Tectonophysics*, *220*(1-4), 89-115.

Baofu, H., Guoqi, H., Shiguang, W., & Dawei, H. (1998). Postcollisional mantle-derived magmatism and vertical growth of the continental crust in north Xinjiang. *Geological Review*, *44*(4), 396-406.

Bazhenov, M. L., Collins, A. Q., Degtyarev, K. E., Levashova, N. M., Mikolaichuk, A. V., Pavlov, V. E., & Van der Voo, R. (2003). Paleozoic northward drift of the North Tien Shan (Central Asia) as revealed by Ordovician and Carboniferous paleomagnetism. *Tectonophysics*, 366(1), 113-141.

Boggs Jr, S., & Boggs, S. (2009). Petrology of sedimentary rocks. Cambridge University Press.

Brookfield, M. E. (2000). Geological development and Phanerozoic crustal accretion in the western segment of the southern Tien Shan (Kyrgyzstan, Uzbekistan and Tajikistan). *Tectonophysics*, *328*(1-2), 1-14.

Buchan, C., Pfänder, J., Kröner, A., Brewer, T. S., Tomurtogoo, O., Tomurhuu, D., ... & Windley, B. F. (2002). Timing of accretion and collisional deformation in the Central

Asian Orogenic Belt: implications of granite geochronology in the Bayankhongor Ophiolite Zone. *Chemical Geology*, *192*(1-2), 23-45.

Burtman, V. S. (1975). Structural geology of variscan Tien Shan, USSR. *Am. J. Sci*, *275*, 157-186.

Buslov, M. M., De Grave, J., Bataleva, E. A. V., & Batalev, V. Y. (2007). Cenozoic tectonic and geodynamic evolution of the Kyrgyz Tien Shan Mountains: a review of geological, thermochronological and geophysical data. *Journal of Asian Earth Sciences*, *29*(2-3), 205-214.

Che, Z. C., Liu, H. F., & Liu, L. (1994). Formation and evolution of the middle Tianshan orogenic belt. *Geological Publish House*, Beijing.

Cleven, N. (2011). Fold-and-thrust belt deformation of the Hongliuhe Group: a Permian tectonic closure record of the Central Asian Orogenic Belt, NW China (Master's thesis, University of Waterloo).

Cleven, N. R., Lin, S., & Xiao, W. (2015). The Hongliuhe fold-and-thrust belt: evidence of terminal collision and suture-reactivation after the Early Permian in the Beishan orogenic collage, Northwest China. *Gondwana Research*, *27*(2), 796-810.

Cleven, N. R., Lin, S., Xiao, W., Davis, D. W., & Davis, B. (2017). Successive arc accretion in the southern Central Asian orogenic belt, NW China: Evidence from two Paleozoic arcs with offset magmatic periods. Bulletin, 130(3-4), 537-557.

Coleman, R. G. (1989). Continental growth of northwest China. *Tectonics*, 8(3), 621-635.

Coward, M. P. (1994). Inversion tectonics. Continental deformation, 289-304.

Cross, T. A. (1986). Tectonic controls of foreland basin subsidence and Laramide style deformation, western United States. *Foreland basins*, 13-39.

Dickinson, W. R. (1985). Interpreting provenance relations from detrital modes of sandstones. In Provenance *of arenites* (pp. 333-361). Springer, Dordrecht.

Dobretsov, N. L., Berzin, N. A., & Buslov, M. M. (1995). Opening and tectonic evolution of the Paleo-Asian Ocean. *International Geology Review*, 37(4), 335-360.

Festa, A., Ogata, K., Pini, G. A., Dilek, Y., & Alonso, J. L. (2016). Origin and significance of olistostromes in the evolution of orogenic belts: A global synthesis. *Gondwana Research*, *39*, 180-203.

Gansu Bureau of Geology and Mineral Resources (Gansu BGMR), 1966. Regional Geology of the Gansu Jiuquan Region. *Geological Publishing House*, Beijing, p. 157 (in Chinese with English abstract)

Guo, Q., Xiao, W., Windley, B. F., Mao, Q., Han, C., Qu, J., ... & Yong, Y. (2012). Provenance and tectonic settings of Permian turbidites from the Beishan Mountains, NW China: implications for the Late Paleozoic accretionary tectonics of the southern Altaids. *Journal of Asian Earth Sciences*, 49, 54-68.

Hu, J., Liu, X., Li, Z., Zhao, Y., Zhang, S., Liu, X., ... & Chen, H. (2013). SHRIMP U-Pb zircon dating of the Ordos Basin basement and its tectonic significance. Chinese Science Bulletin, 58(1), 118-127.

Ingersoll, R. V. (2011). Tectonics of sedimentary basins, with revised nomenclature. Tectonics of sedimentary basins: Recent advances, 1-43.

Jun, G., Maosong, L., Xuchang, X., Yaoqing, T., & Guoqi, H. (1998). Paleozoic tectonic evolution of the Tianshan Orogen, northwestern China. *Tectonophysics*, *287*(1-4), 213-231.

Liao, Z.T., Liu, L.J., 2003. The Carboniferous and Permian of the Gansu–Xinjiang border area with remarks on the age of the surrounding strata of the Jinwozi gold ore. *Journal of Stratigraphy* 27, 163–172 (in Chinese with English abstract).

Liu, X., Chen, B., Jahn, B. M., Wu, G., & Liu, Y. (2011). Early Paleozoic (ca. 465 Ma) eclogites from Beishan (NW China) and their bearing on the tectonic evolution of the southern Central Asian Orogenic Belt. Journal of Asian Earth Sciences, 42(4), 715-731.

Mao, Q., Xiao, W., Fang, T., Wang, J., Han, C., Sun, M., & Yuan, C. (2012 a). Late Ordovician to early Devonian adakites and Nb-enriched basalts in the Liuyuan area, Beishan, NW China: implications for early Paleozoic slab-melting and crustal growth in the southern Altaids. *Gondwana Research*, *22*(2), 534-553.

Mao, Q., Xiao, W., Windley, B. F., Han, C., Qu, J., Ao, S., ... & Guo, Q. (2012 b). The Liuyuan complex in the Beishan, NW China: a Carboniferous–Permian ophiolitic fore-arc sliver in the southern Altaids. *Geological Magazine*, 149(3), 483-506.

Pini, G. A. (1999). Tectonosomes and olistostromes in the Argille Scagliose of the Northern Apennines, Italy (Vol. 335). Geological Society of America.

Prothero, D. R., & Schwab, F. (1996). Sedimentary Geology WH Freeman and Company. New York, p575.

Qu, J. F., Xiao, W. J., Windley, B. F., Han, C. M., Mao, Q. G., Ao, S. J., & Zhang, J. E. (2011). Ordovician eclogites from the Chinese Beishan: implications for the tectonic evolution of the southern Altaids. *Journal of Metamorphic Geology*, *29*(8), 803-820.

Sengör, A. C., & Natal'In, B. A. (1996). Turkic-type orogeny and its role in the making of the continental crust. *Annual Review of Earth and Planetary Sciences*, *24*(1), 263-337.

Şengör, A. M. C., Natal'In, B. A., & Burtman, V. S. (1993). Evolution of the Altaid tectonic collage and Palaeozoic crustal growth in Eurasia. *Nature*, *364*(6435), 299.

Van Staal, C., Hong, T., Lin, S. F., Ji, W. H., Kang, L., & Yang, J. G. (2018) Guide Book for Field Excursion of First Workshop of Project IGCP-662 “Orogenic architecture and crustal growth from accretion to collision”. Not published.

Wang, B. Y., Lang, Z., Li, X., Qu, X., Li, T., Huang, C., & Cui, X. (1994). Comprehensive survey of geological sections in the west Tianshan of Xinjiang, China. *Science in China Press, Beijing*, *202*.

Wang, Y., Luo, Z., Santosh, M., Wang, S., & Wang, N. (2017). The Liuyuan Volcanic Belt in NW China revisited: evidence for Permian rifting associated with the assembly of continental blocks in the Central Asian Orogenic Belt. *Geological Magazine*, *154*(2), 265-285.

Windley, B. F., Alexeiev, D., Xiao, W., Kröner, A., & Badarch, G. (2007). Tectonic models for accretion of the Central Asian Orogenic Belt. *Journal of the Geological Society*, *164*(1), 31-47.

Windley, B. F., Allen, M. B., Zhang, C., Zhao, Z. Y., & Wang, G. R. (1990). Paleozoic accretion and Cenozoic redeformation of the Chinese Tien Shan range, central Asia. *Geology*, *18*(2), 128-131.

Xiao, W., Han, C., Yuan, C., Sun, M., Lin, S., Chen, H., ... & Sun, S. (2008). Middle Cambrian to Permian subduction-related accretionary orogenesis of Northern Xinjiang, NW China: implications for the tectonic evolution of central Asia. *Journal of Asian Earth Sciences*, *32*(2-4), 102-117.

Xiao, W., Huang, B., Han, C., Sun, S., & Li, J. (2010b). A review of the western part of the Altaids: a key to understanding the architecture of accretionary orogens. *Gondwana Research*, *18*(2-3), 253-273.

Xiao, W. J., Mao, Q. G., Windley, B. F., Han, C. M., Qu, J. F., Zhang, J. E., ... & Shan, Y. H. (2010a). Paleozoic multiple accretionary and collisional processes of the Beishan orogenic collage. *American Journal of Science*, *310*(10), 1553-1594.

Xiao, W. J., Zhang, L. C., Qin, K. Z., Sun, S. H. U., & Li, J. L. (2004a). Paleozoic accretionary and collisional tectonics of the Eastern Tianshan (China): implications for the continental growth of central Asia. *American Journal of Science*, *304*(4), 370-395.

Xiao, W., Windley, B. F., Badarch, G., Sun, S., Li, J., Qin, K., & Wang, Z. (2004b). Palaeozoic accretionary and convergent tectonics of the southern Altaids: implications for the growth of Central Asia. *Journal of the Geological Society*, *161*(3), 339-342.

Xiao, W., Windley, B. F., Hao, J., & Zhai, M. (2003). Accretion leading to collision and the Permian Solonker suture, Inner Mongolia, China: termination of the central Asian orogenic belt. *Tectonics*, 22(6).

Xiao, W. J., Windley, B. F., Huang, B. C., Han, C. M., Yuan, C., Chen, H. L., ... & Li, J. L. (2009a). End-Permian to mid-Triassic termination of the accretionary processes of the southern Altaids: implications for the geodynamic evolution, Phanerozoic continental

growth, and metallogeny of Central Asia. *International Journal of Earth Sciences*, *98*(6), 1189-1217.

Xiao, W. J., Windley, B. F., Yuan, C., Sun, M., Han, C. M., Lin, S. F., ... & Li, J. L. (2009b). Paleozoic multiple subduction-accretion processes of the southern Altaids. *American Journal of Science*, *309*(3), 221-270.

Zhao, Z. H., Guo, Z. J., Han, B. F., Wang, Y, and Liu, C., 2006a, Comparative study on Permian basalts from the Beishan area, eastern Xinjiang Uygur Autonomous Region and Gansu Province, and its tectonic significance: *Acta Petrologica Sinica*, v. 22, n. 5, p. 1279–1293 (in Chinese with English abstract).

Zhou, D., Su, L., Jian, P., Wang, R., Liu, X., Lu, G., & Wang, J. (2004). Zircon U-Pb SHRIMP ages of high-pressure granulite in Yushugou ophiolitic terrane in southern Tianshan and their tectonic implications. *Chinese Science Bulletin*, *49*(13), 1415.

Zuo, G., Zhang, S., He, G., and Zhang, Y., 1990, Early Paleozoic plate tectonics in Beishan area: *Scientia Geologica Sinica*, v. 4, p. 305–314

Zuo, G., Zhang, S., He, G., and Zhang, Y., 1991, Plate tectonic characteristics during the early Paleozoic in Beishan near the Sino-Mongolian border region, China: *Tectonophysics*, v. 188, n. 3–4, p. 385–392, doi:10.1016/0040-1951(91)90466-6

Zuo, G. C., Liu, Y. K., & Liu, C. Y. (2003). Framework and evolution of the tectonic structure in Beishan area across Gansu Province, Xinjiang Autonomous region and Inner Mongolia Autonomous Region. *Acta Geologica Gansu*, *12*(1), 1-15.